Evidence of gravity wave contribution to vertical shear and mixing in the lower stratosphere

Madhuri Umbarkar[1], Daniel Kunkel[1], Annette Miltenberger[1], Hans-Christoph Lachnitt[1], Thorsten Kaluza[2], Cornelis Schwenk[1], and Peter Hoor[1]

[1]Institute for Atmospheric Physics, Johannes Gutenberg University Mainz, Germany
[2]Department of Meteorology, University of Reading, Reading, UK

Correspondence: Madhuri Umbarkar (mumbarka@uni-mainz.de)

Abstract. Evidence is presented which illustrates the role of atmospheric gravity wave (GW) induced shear as a mechanism for the occurrence of clear air turbulence and mixing of air masses with different chemical composition in the lower stratosphere. This study investigates the relation of GWs, vertical wind shear and turbulence as well as the potential consequence of this relation onto the trace species distribution in the lowermost stratosphere (LMS) over the North Atlantic. The analysis of airborne observations, reanalysis and forecast data highlight the impact of mesoscale dynamics in relation to GWs on the constituents around the tropopause. The GWs propagate through highly sheared flow above the jet stream maximum, perturbing background wind shear and static stability, and thereby creating conditions conducive to turbulent mixing in the LMS. The observed significant correlation between GW-induced momentum flux and enhanced shear perturbations confirms the role of GWs in driving potential turbulence and facilitating trace gas exchange. Further analysis of turbulence diagnostics including gradient Richardson number on large-scale and turbulence indices (TI1, TI2) on small-scale suggests that GWs produce shear which leads to the occurrence of clear air turbulence. In summary, this study extends the findings from idealized experiments as shown in Umbarkar and Kunkel (2025) to the 'real' world and provide physical and chemical evidence of the role of small-scale processes in the dynamics and composition of the tropopause region.

1 Introduction

Atmospheric gravity waves (GW), ubiquitous buoyancy-driven oscillations, play a crucial role in a wide variety of atmospheric processes. These gravity waves can initiate and organize convection (Zhang et al., 2001), as well as generate and modulate atmospheric turbulence (Shapiro, 1980). Also, GWs redistribute momentum and energy through vertical propagation, which affects the general circulation, particularly in the upper atmosphere but also the exchange of air masses between troposphere and stratosphere (Holton et al., 1995).

Generally speaking, GWs can be generated and activated by topographic forcing, convection, shear instability, as well as geostrophic adjustment related to jets, fronts, and sources of strong diabatic heating (Hooke, 1986; Fritts and Alexander, 2003; Kim et al., 2003; Plougonven et al., 2008). Orographic GWs are generated through the interaction between atmospheric flow and surface topographic features, producing mainly vertically propagating waves that influence the energy and momentum

balance in the UTLS (Durran, 1995; Lachnitt et al., 2023). These GWs propagate further upwards through the stratosphere where they dissipate and influence the atmospheric circulation, particularly the Brewer-Dobson circulation (Achatz et al., 2024, and references therein). Convective sources generate GWs through latent heat release and rapid vertical motions as in thunderstorms, often observed in both tropical and extratropical regions (Fritts and Alexander, 2003; Alexander et al., 2010). Moreover, Lane et al. (2001) and Lane and Sharman (2006) emphasized that convective clouds generate GWs when the convective updraft rapidly decelerates. The distribution of different GW sources largely controls the global distribution of GWs and their impact on atmospheric stability and transport processes.

In the extratropics, baroclinic life cycles represent an important, albeit less well understood, source of GWs. Baroclinic waves exhibit finer-scale substructures, such as upper- and lower-level fronts, convective ascent, jet streaks and flow imbalances, that are susceptible for GW excitation, primarily through spontaneous imbalance, whereby deviations from balanced flow trigger wave emission (Plougonven and Zhang, 2014; Zhang et al., 2015b). Regions of baroclinic instability, particularly along jet streaks and frontal zones, are hotspots for non-orographic GW activity. Moreover, tropospheric moist processes turn out to play an important role in the generation of GW from mid-latitude and high-latitude weather systems (e.g. Wei and Zhang, 2014; Plougonven et al., 2015; Holt et al., 2017). In such regions, interactions between divergent flow (or GWs) and the background flow (Trier et al., 2020) lead to shear generation and turbulence (e.g., O'sullivan and Dunkerton, 1995; Plougonven and Snyder, 2005; Zülicke and Peters, 2006; Kaluza et al., 2021). GWs excited from tropospheric weather systems (or synoptic eddies) can propagate into the UTLS and middle atmosphere. Upon dissipation, these waves deposit momentum and energy and consequently contribute to driving the Brewer–Dobson circulation (Alexander et al., 2010; Achatz et al., 2024, and references therein). Additionally, around the the tropopause GWs from baroclinic systems affect the dynamic and thermodynamic structure (Plougonven et al., 2008; Dörnbrack, 2024; Jovanovic, 2025). However, despite the ubiquity of these GWs, the generation mechanisms of these GWs remains poorly understood.

On the other hand orographic GWs, despite their significant seasonality and high degree of transience, often lead to turbulence at the tropopause (Fritts and Alexander, 2003; Alexander and Grimsdell, 2013; Rapp et al., 2021). As an example, Lachnitt et al. (2023) highlighted that GW induced turbulence can persistently affect the distribution of trace species in the lower stratosphere. Such processes affect the isentropic gradients of radiation active trace species (e.g., Dörnbrack et al., 2025) and as such contribute to the overall mixing-induced uncertainty of radiative forcing (Riese et al., 2012).

GWs induce fluctuations of key state variables on the background state and as such affect vertical wind shear and static stability of the tropopause region (Kunkel et al., 2016; Kaluza et al., 2021; Dörnbrack, 2024). In case of GW dissipation or breaking, these initially reversible fluctuations can lead to irreversible mixing and GW flux convergence which modifies the background state on longer time scales. Ultimately, this can foster the formation of a layer of enhanced shear in the extratropics, the so called "tropopause shear layer" (TSL, Kaluza et al., 2021). The TSL is typically identified as the region near the extratropical tropopause where shear exceeds a critical threshold S_t^2, typically the 95$^{\text{th}}$ percentile of climatological dataset. Such enhanced shear is often linked to tropopause disturbances and has been observed on the order of 10^{-2}–$10^{-3}\,\text{s}^{-1}$ (Lane et al., 2004; Kaluza et al., 2021), occurring particularly in dynamically active regions such as jet streaks and frontal zones and often in combination with clear air turbulence (Koch et al., 2005; Wang and Zhang, 2007). Large vertical shear in

the lower stratosphere is often associated with enhanced static stability in this region. Partly, the enhanced static stability is a consequence of dissipating GWs in the this region (Kunkel et al., 2014; Zhang et al., 2015b). It has further been shown through the analysis of aircraft and observations and model simulations that irreversible mixing occurs in these regions (Kunkel et al., 2019). However, such analyses are still limited, partly through the sparse observational data sets and through the need of very high resolution models to correctly capture the relevant processes (Plougonven and Zhang, 2014; Stephan et al., 2019a; Geller et al., 2013; Jewtoukoff et al., 2015).

GWs influence tracer transport and mixing in the UTLS by generating turbulence, either through enhanced vertical shear that triggers instabilities like Kelvin–Helmholtz instability or through wave breaking at critical levels where GW phase speed aligns with the background wind (e.g., Shapiro, 1978; Whiteway et al., 2004; Lane and Sharman, 2006). As such GWs contribute to the formation of the extratropical transition layer (ExTL), which is a region around the extratropical tropopause which from a tracer based perspective represents a transition zone between stratospheric and tropospheric air masses (Hoor et al., 2004; Pan et al., 2006; Hegglin et al., 2009). The ExTL resides to a large degree in the lower part of the lowermost stratosphere (LMS). While the ExTL is situated around the extratropical tropopause, usually defined as an isosurface of potential vorticity, the LMS is the region between the extratropical and the tropical tropopause, bounded above by the 380 K isentrope (Weyland et al., 2025; Appenzeller et al., 1996; Holton et al., 1995; Olsen et al., 2013; Wang and Fu, 2021). Chemical species with origins in either the troposphere, e.g., water vapor or carbon monoxide, or in the stratosphere, e.g., ozone, exhibit strong vertical changes in the ExTL and LMS. This is partly the result of the distribution of the source regions as well as of chemical processes of the respective species but also most importantly of dynamical processes in the stratosphere and troposphere. In the extratropics, quasi-isentropic transport is crucial on the one hand to mix air masses between troposphere and stratosphere and within the stratosphere as has been shown by trajectory-based analyses (Berthet et al., 2007; Hoor et al., 2010) and by airborne observations (e.g., Hoor et al., 2004; Pan et al., 2004; Kunkel et al., 2019). On the other side, small–scale processes foster mixing more locally, often in relation to shear instabilities or convection (e.g., Whiteway et al., 2003; Lane et al., 2004; Zhang et al., 2015b; Lachnitt et al., 2023; Dörnbrack et al., 2025). As such the composition of the ExTL depends on GWs which in turn affects the radiative balance in the extratropical UTLS (Birner et al., 2002; Birner, 2006; Hoor et al., 2004; Zhang et al., 2015a; Heller et al., 2017).

A particular interesting turbulence which occurs in the lower stratosphere is induced by shear and often occurs in clear sky conditions. The identification of this clear air turbulence (CAT) is crucial for safety aspects in commercial aviation as well as for mixing of trace species and as such the chemical composition in the UTLS (Chau et al., 2025, 2026). Simulations of midlatitude cyclones highlight the role of jet dynamics and GWs in CAT generation (Lane et al., 2004; Trier et al., 2020). In addition to vertical shear–based diagnostics (e.g. gradient Richardson number), empirical turbulence indices such as TI1 and TI2 are widely used in CAT identification (Ellrod and Knapp, 1992; Sharman et al., 2006; Jaeger and Sprenger, 2007). However, forecasting CAT remains challenging due to its intermittent nature and small–scale motion with turbulent eddies typically spanning horizontal scales of $\sim$10 to 1000 m compared to the resolution of current numerical weather prediction models (Sharman et al., 2006, 2014; Sharman and Pearson, 2017). More so, it is important to analyse the sources of this turbulence, as GW and shear are important factors that can promote its development.

Our primary goal of this study is based on recent revelations from idealized simulations of baroclinic life cycles (Umbarkar and Kunkel, 2025). In these simulations, a clear relation between GWs, enhanced shear and potential turbulence occurrence in the lower stratosphere was found. The question is now whether this relation is also evident within an extratropical life cycle over the North Atlantic. First, we present evidence from observations of recent mixing between chemically different air masses during a flight of the WISE (Wave-driven ISentropic Exchange) mission in September 2017. We further examine whether this mixing event is linked to enhanced shear and GW activity (Sect. 3). Second, we examine the representation of shear and the associated GW-induced turbulent mixing in ERA5 reanalysis fields over a larger domain over the North Atlantic during this event in the UTLS (Sect. 4). After that we put our results from the reanalysis data into perspective, once compared to IFS forecast data, and then to ICON forecasts on varying resolutions (Sect. 5). The last point is related to the question which aspects of the GW field can be reliably investigated in ERA5 fields, given their resolution, and whether the resolved spectrum of GWs is enough to study their impact on shear and mixing in the UTLS in case studies, and thus potentially may be suited for climatological analyses on this topic. Furthermore, we also investigate whether instabilities triggered by GW-induced shear can lead to the development of CAT.

2 Data and methods

2.1 In situ measurements

In autumn 2017, the WISE (Wave-driven ISentropic Exchange) mission was conducted using the German HALO (High Altitude and Long Range) research aircraft, operating from Oberpfaffenhofen, Germany, and Shannon, Ireland. In this study we focus on research flight 05 on 23rd September 2017 between 08:09 and 17:04 UTC. The goal of this flight was to investigate the dynamical and chemical structure of the atmosphere in the vicinity of the tropopause over the North Atlantic between Ireland and a region north of Iceland in a far north reaching subtropical intrusion.

During the WISE campaign, HALO was outfitted with a specialized suite of instruments for in situ and remote sensing. Our analysis is mainly based on in-situ measurement of CO and N_2O from UMAQS (University of Mainz Airborne Quantum Cascade Laser Spectrometer, Müller et al., 2015). For the WISE campaign, the total drift-corrected uncertainty was determined to be 0.94 ppbv for CO and 0.18 ppbv for N_2O (Kunkel et al., 2019). Additionally, we use meteorological parameters measured with BAHAMAS (Basic HALO Measurement and Sensor System, Krautstrunk and Giez, 2012; Kunkel et al., 2019).

2.2 ERA5 reanalysis data

As a reference for the zonal and meridional wind components and as the basis for additional meteorological context, ERA5 the most recent reanalysis produced by the European Center for Medium-Range Weather Forecasts 5th generation (ECMWF, Hersbach et al., 2020) is used. It is based on 4DVar data assimilation and model forecast using cycle Cy41r2 of the ECMWF Integrated Forecasting System (IFS) model. The model data is available on 137 model levels from the surface to 0.01 hPa with a vertical grid spacing of roughly 300 m in the UTLS. The model level data has further been interpolated on height, pressure

and isentropic levels for our analysis. In this study, two ERA5 based products are used: (i) data extracted along the flight path used in Sect. 3 (Lachnitt, 2025) and (ii) four-dimensional meteorological fields with hourly time resolution and on horizontal grid with 0.25° in latitude and longitude, used in Sect. 4.

2.3 IFS forecast

Next, we use ECMWF IFS operational forecast data as a high resolution companion of the ERA5 reanalysis. The data is based on IFS cycle 43r3 and analyzed on a regular 0.1° latitude-longitude grid with hourly temporal resolution. This data is of interest because the IFS version used to produce this forecast is very close to the version used for ERA5 production. The operational IFS employs a Tco1279 spectral truncation and an associated O1280 octahedral grid which results in an $\Delta x \approx 9$ km grid spacing in the horizontal and incorporates 137 vertical levels which are the same vertical resolution used in reanalysis and in forecasts. This data has almost the same dynamical core and physical package as ERA5 which allows to study the effect of higher horizontal resolution on the representation of shear and GWs. We use the operational forecast from 23 September 2017 00:00 UTC, with hourly resolution for the first 24 hours of this forecast.

2.4 ICON forecast

In addition, we use forecast data of this case from Schwenk and Miltenberger (2024) who used version 2.6.2 of the ICOsahedral Nonhydrostatic (ICON) modeling framework (Zängl et al., 2014) over the North Atlantic Ocean. This allows us to study the representation of the same situation in a model with a different dynamical core and physics package as well as in three different resolutions from roughly the resolution of the IFS data to almost convection permitting resolution. We can then directly test how robust our findings are across different model representations. The simulation was initialized with the operational global

Table 1. Summary of physics parameterization schemes used for ICON simulations

Physics	**Schemes used**
Convection	Tiedtke–Bechtold convection scheme (13 km)
	only shallow convection (6.5 km, 3.3 km)
Non-orographic gravity wave drag	Orr et al. (2010)
Sub-grid scale orographic drag	Lott and Miller (1997)
Turbulence	Raschendorfer (2001)
Radiation	Rapid Radiative Transfer Model
Cloud microphysics	two-moment microphysics (Seifert, 2008)

ICON analysis at 00:00 UTC on 20 September 2017, shortly before the cyclone developed, and ran for 96 hours, ending at 00:00 UTC on 24 September 2017, when the life cycle of cyclone was in its final stage (Schwenk and Miltenberger, 2024). The global ICON model simulation applied a R03B07 grid (effective resolution of ∼13 km) with a 120 s time step, contained

to nested regions using R03B08 (∼6.5 km) and R03B09 (∼3.3 km) grids with 60 s and 30 s time steps, respectively (Fig. A3). In the vertical the ICON simulations have 90 levels from the surface up to 23 km altitude with a vertical grid spacing of roughly 250–300 m in the UTLS. Figure 1 illustrates the ICON nested setup and atmospheric situation over the study region using ERA5 at 11:00 UTC on 23 September 2017. More details about the physics parameterization schemes used for ICON simulations are given in Table 1.

2.5 Deriving resolved gravity wave momentum fluxes and turbulence diagnostics

For the analysis of GWs and turbulence from model fields, we follow the approach outlined in Umbarkar and Kunkel (2025) with some extensions. We outline the most important aspects here briefly. First of all, GWs manifest in small–scale deviations from the background state and we use a hybrid method combining a dynamical with a statistical approach to separate between the (large–scale) background and the (small–scale) deviations (similar to Wei et al., 2022). Note that we define the large–scale flow here as background. We first divide the flow in its divergent and rotational components through the application of a Helmholtz decomposition, i.e., the dynamical approach. For the so called statistical component, we then apply a spectral filter using a one-dimensional zonal FFT over the full domain displayed in Fig. 1. Thus, we remove the contributions from wavenumber 0 to 20, i.e. $u' = u_{\mathrm{div}} - (u_{\mathrm{div}})_{k \le k_s}$, where k_s = 20, is the wavenumber cutoff that splits respective quantities into a large–scale and small–scale components. The primes ($'$) mark from now on the deviations from the background state. Note here that sensitivity tests with k_s values of $\pm$ 4 showed no significant variation in the resulting primed quantities. The deviation of small–scale from large–scale flow are shown in Fig. A1.

We identify GWs once based on the horizontal divergence $\nabla_h \cdot u_h$ (e.g., Kunkel et al., 2014). Additionally, we use the absolute momentum flux

$$\mathrm{AMF} = \rho \sqrt{(\overline{u'w'})^2 + (\overline{v'w'})^2} \tag{1}$$

where ρ is the mean density, and u', v', and w' are the zonal, meridional, and vertical velocity perturbations, respectively. The overline over the perturbation products (i.e. $\overline{u'w'}$ and $\overline{v'w'}$) highlights a low-pass filtering of the quadratic quantities using the same Gaussian spectral filter as in Kruse and Smith (2015). We use the *AMF* as a first proxy for the momentum flux due to small-scales and as such to GWs.

A recent study by Zhang et al. (2025) suggests that the hybrid scale-separation approach is applicable in the lowermost stratosphere (e.g., around 200 hPa). Moreover, Wei et al. (2022); Zhang et al. (2025) further suggest that using the divergent wind to separate the GW flow from the background gives more reliable estimates of GW momentum flux, particularly in the upper troposphere.Thus, we emphasize here that our hybrid approach to seperate the scales of the flow is well justified in the UTLS (Zhang et al., 2025) and follows the commonly used GW scale separation methods as in Lehmann et al. (2012); Wei et al. (2016); Stephan et al. (2019a); Strube et al. (2020); Gupta et al. (2021); Wei et al. (2022); Umbarkar and Kunkel (2025), despite different cutoff wavenumber being used in different studies. Nevertheless, in this study, the focus is primarily on the lowermost stratosphere, where the scale separation is comparatively more robust, and the limitations of the method are therefore reduced.

Beside the GW diagnostics, we use several other quantities to analyze whether the flow is prone to turbulence occurrence. A key diagnostics is the vertical shear:

$$S^2 = \left(\frac{\partial u}{\partial z}\right)^2 + \left(\frac{\partial v}{\partial z}\right)^2. \tag{2}$$

While S^2 is derived with the full wind, it will also be calculated from the wind perturbations ($S^{2'}$). Furthermore, we use the gradient Richardson number *Ri* and the Ellord turbulence indices, TI1 and TI2 to estimate whether the flow is turbulent or not Sharman et al. (2006). The use of multiple diagnostics is motivated by the need to capture both dynamical and kinematic aspects of turbulence generation in the extratropical UTLS, especially to asses the regions affected by GW-induced shear and mixing. Here, dynamical diagnostics characterize the stratification of the flow and its susceptibility to instabilities, whereas kinematic diagnostics describe flow deformation and shear that can promote turbulence development. *Ri* is calculated as follows:

$$Ri = \frac{N^2}{S^2} = \frac{\left(\frac{g}{\theta}\frac{\partial \theta}{\partial z}\right)}{\left(\frac{\partial u}{\partial z}\right)^2 + \left(\frac{\partial v}{\partial z}\right)^2} \tag{3}$$

i.e., the ratio of static stability (N^2) to vertical wind shear (S^2). It is often assumed that a *Ri* below a critical value result is required for a Kelvin-Helmholtz instability. The critical value for linear shear instability of an idealized stratified flow is often determined to be 0.25, but for analyses using model quantities a value on the order of 1 is considered to mark regions prone for Kelvin-Helmholtz instabilities (e.g., Kunkel et al., 2019). Note that the total vertical wind shear is used to compute *Ri*, in order to initially evaluate regions susceptible to turbulence within the baroclinic flow.

Additionally to *Ri*, we use the Ellord-Knapp turbulence indices, TI1 and TI2, which are empirical diagnostics specifically developed to identify CAT, to better represent turbulence under complex flow conditions. The TI1 has previously been shown to be capable of detecting 70%–84% of CAT occurrences (e.g., Ellrod and Knapp, 1992; Sharman and Pearson, 2017; Kim et al., 2018; Gultepe et al., 2019; Thompson and Schultz, 2021). We resort this to the small-scales, ensuring that potential turbulence in the subsequent analysis reflects subgrid or small–scale contributions. We note here that Kelvin-Helmholtz instability and turbulence are not explicitly resolved in the used reanalyses as well as forecast even if the GWs themselves are. While these processes are represented through subgrid-scale parameterizations, our analysis uses diagnostics based on the resolved fields in ERA5, IFS and ICON. These diagnostics highlight regions with favourable conditions for turbulence occurrence. Following Ellrod and Knapp (1992), the TI1 combines vertical wind shear perturbations and the total flow deformation (DEF), whereas TI2 adds additionally a convergence (CVG) term.The TI1 is calculated as

$$\mathrm{TI1} = \mathrm{S} \times \mathrm{DEF} \tag{4}$$

and the TI2 as:

$$\mathrm{TI2} = \mathrm{S} \times (\mathrm{DEF} + \mathrm{CVG}) \tag{5}$$

where S is the magnitude of vertical wind shear perturbations ($S^{2'}$, see Eq. 2). DEF is the total flow deformation:

$$\mathrm{DEF} = \left(\left(\frac{\partial u}{\partial x} - \frac{\partial v}{\partial y}\right)^2 + \left(\frac{\partial v}{\partial x} + \frac{\partial u}{\partial y}\right)^2\right)^{1/2} \tag{6}$$

and convergence is calculated according to,

$$\mathrm{CVG} = -\left(\frac{\partial u}{\partial x} + \frac{\partial v}{\partial y}\right) \tag{7}$$

Here, both CVG and DEF are consistently derived from the perturbation wind components (u', v'), and thus TI1 and TI2 are likewise based only on the corresponding prime quantities. The inclusion of CVG in TI2 offers an advantage over TI1 by capturing the small–scale flow features such as those associated with GWs or upper level frontal structures. These region often exhibit enhanced shear and convergence making TI2 more sensitive to turbulence driven by mixing processes.

3 Analysis of GW induced mixing in a baroclinic wave over Iceland

3.1 Meteorological situation

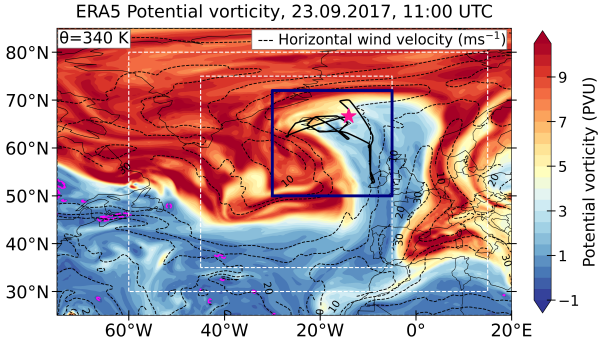


Figure 1. Potential vorticity distribution (in PVU) at the 340 K isentropic surface on 23.09.2017 at 11:00 UTC for ERA5 reanalysis data. The dashed lines show the horizontal wind (in m s^{-1}) on 340 K. The thick black line shows the flight path of research flight 05 and the star marks the aircraft position at 11:00 UTC. Magenta color shows negative PV values which are often related to cloud processes.

The major goal of the flight was to determine whether trace species show specific signatures of irreversible mixing in regions of enhanced static stability in the lower stratosphere. We took advantage of this flight data and further ask whether this irreversible mixing event occurs in regions of GW-induced shear enhancement. The flight was planned in the ridge of a synoptic-scale baroclinic wave which evolved during the previous days over the North Atlantic at the edge of large–scale trough.

The isentropic distribution of potential vorticity on 340 K in Fig. 1 illustrates the meteorological situation during research flight number 5 of the WISE campaign (in following denoted as WISE RF05) for ERA5 reanalysis fields. A strong meridional excursion of the sub-tropical air masses far north in a region from the Iberian peninsula over Great Britain up to Iceland dominates the synoptic situation on 23. September 2017 at 11:00 UTC over the North Atlantic Ocean. Adjacent to the tropospheric streamer two equatorward reaching stratospheric streamers are present, the one to the west being more coherent in its structure, while the one to the east shows more internal structure in terms of its isentropic PV.

The flight went from Shannon, Ireland towards Iceland where a hexagon was flown as well as a dive was performed before returning to Shannon (see black line in Fig. 1). The PV distribution shows that the flight took place to a large degree in the region where subtropical air masses, around 11–13 km, moved polewards while some parts of the flight track also reached
230 across the PV gradient into the lower stratosphere. The region of the strong PV gradient corresponds to the location of the jet stream and acts as a barrier between tropospheric and stratospheric air masses. On the large–scale, IFS (Fig. A2) and ICON (Fig. A3) forecasts show similar patterns in terms of the overall PV distribution. Moreover, smaller-scale ripple-like structures in the PV field around 20° W and 65° N (Fig. 1) could signify wave activity similar to the another case during WISE (Kunkel et al., 2019). Such small–scale structures in the PV field could already hint towards the presence of GWs associated with
235 mixing of air masses.

3.2 Identification of flight segments affected by turbulence

Next, we examine the time series of measured and ERA5 derived quantities during WISE RF05. The goal is to identify regions and periods of potential turbulence and small–scale mixing above the tropopause.

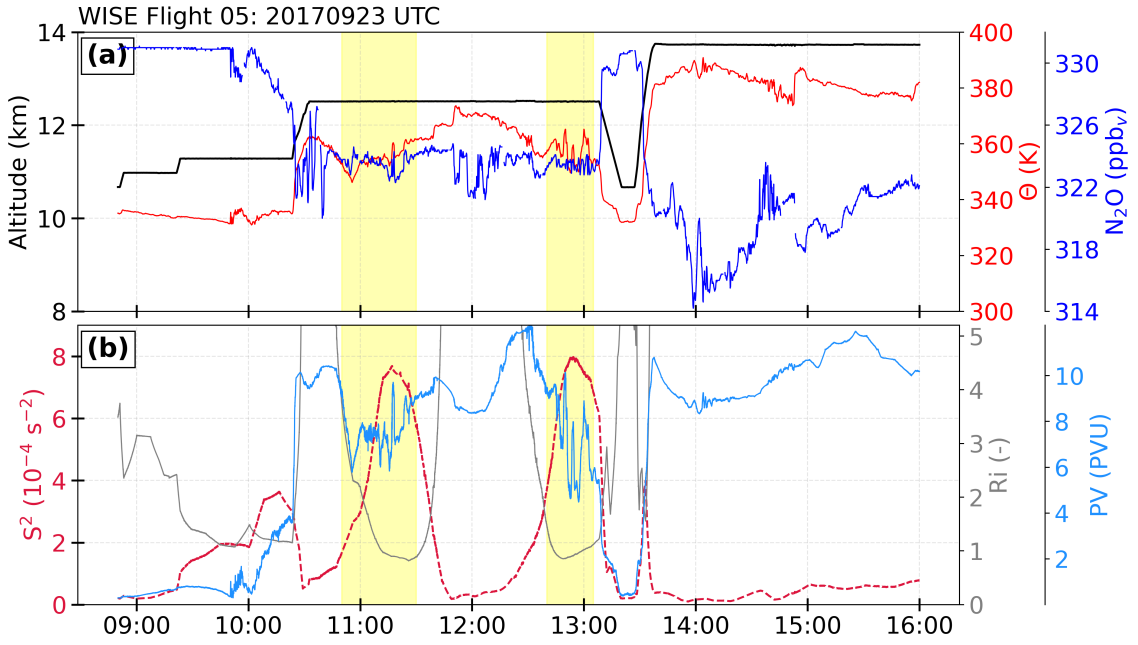


Figure 2. Time series of (a) observed flight altitude (in km, black), potential temperature (in K, red), and nitrous oxide (in ppbv, blue) as well as (b) ERA5 derived quantities along the flight path such as vertical shear (in 10^{-4} s^{-2}, red), Richardson number (dimensionless, grey), and potential vorticity (in PVU, cyan). The light yellow bars and the white bar in between indicate the flight section of the consecutive detailed analysis of mixed air masses.

Figure 2 shows a comparison of in situ measured atmospheric state parameters including chemical tracers and potential temperature (a) and instability parameters (b) from the ERA5 reanalysis data that was interpolated in time and space onto the flight path. The pressure altitude measured during WISE RF05 shows that the flight path was designed to ascend with time (Fig 2a). An exception is the dive between 13:00 UTC and 14:00 UTC. This ascent is also mirrored in the decrease of N_2O with time and the associated increase of potential temperature and ERA5 potential vorticity. In contrast, ERA5 vertical shear S^2 and Richardson number *Ri* show a more diverse temporal evolution. In particular, two shear maxima are evident with values reaching up to $8 \times 10^{-4}\,s^{-2}$ which are associated with minima in *Ri* below 1 (Fig. 2b). Compared to other times during the flight, these two time periods stand out in terms of high shear values and low *Ri*.

3.3 Trace gas observations, the role of gravity waves and small–scale mixing

We use tracer-tracer correlations and vertical trace species profiles to further examine the time periods which showed indications of turbulence occurrence. For this we use trace gases suggesting a tropospheric origin on one side, i.e., CO, and trace species indicative of stratospheric air masses, i.e., N_2O on the other side.

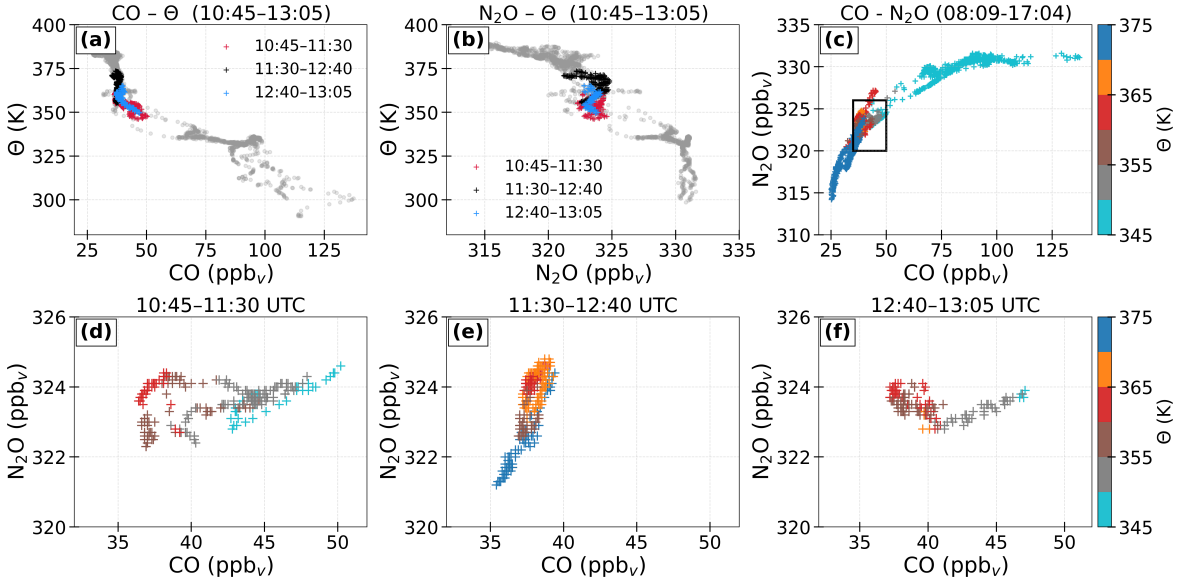


Figure 3. Vertical profiles of (a) CO (in ppbv) and (b) N_2O (in ppbv) with grey circles showing data of the entire flight and color-coded markers indicating the time from 10:45–13:05 UTC. (c-f) Tracer-tracer correlation of the mixing ratios of N_2O and CO for (c) the entire flight and for time periods between (d) 10:45–11:30 UTC, (e) 11:30–12:40 UTC and (f) 12:40–13:05 UTC, color-coded with potential temperature.

We focus on the time period between 10:45 UTC and 13:05 UTC which is the time period bounded by the two yellow marked regions in Fig. 2. During this time HALO was flying in the LMS with potential temperature values between 330 K and below 380 K. The measurements took place just above the region of the strongest vertical gradients of CO and N_2O where the vertical gradient becomes small again (Fig. 3a, b). Since one would generally expect vertical gradients of N_2O over

this potential temperature range, the almost vertical profile is a first indication of a process which mixes or has mixed (i.e. homogenized) air masses prior to the measurements in this altitude range. Additionally, the mixing ratios of CO and N_2O are well below their tropospheric background values, which is also evident in the CO-N_2O correlation (Fig. 3c). The part of the correlation highlighting the time period of interest (marked region) is rather located in the stratospheric branch and partly within the transition region between stratosphere and troposphere. These regions are characterized by low CO and N_2O mixing ratios, with N_2O values below the well-defined tropospheric background of 331 ppbv during WISE RF05 (see also Kunkel et al., 2019). Note that irreversible mixing can be followed from the interrelation of CO, N_2O and potential temperature. Due to the chemical life times of the tracers we can infer that N_2O is almost constant in the troposphere with a sink in the upper stratosphere and thus a minor negative gradient with altitude. The same is true for CO, with the difference that the mixing ratios of CO are less constant in the troposphere and the gradient in the stratosphere is stronger due to stronger chemical sink. However, their tracer-tracer relation is positive. More so, we expect to find a monotonic correlation between CO, N_2O and potential temperature Θ. The mixing ratios of CO and N_2O should decrease as an air mass becomes more stratospheric, whereas potential temperature should simultaneously increase. On first glance this relation is evident in the correlation (Fig. 3c) and profiles shown in Fig. 2. While both tracers decrease with altitude, potential temperature increases, which in turn gives specific background relation of these three species. A deviation from the stated background condition is then only possible in the presence of non-conservative processes. Recent analyses highlighted the role of GWs in such situations and the consequent irreversible mixing of trace species (e.g., Kunkel et al., 2019; Lachnitt et al., 2023).

For further analysis, we split the correlation into three periods: (i) 10:45–11:30 UTC (Fig. 3d), (ii) 11:30–12:40 UTC (Fig. 3e), and (iii) 12:40–13:05 UTC (Fig. 3f). Several interesting features emerge. The first period exhibits two branches connected by a mixing line (around $N_2O \sim 324$ ppbv and $\Theta \sim 359$ K). During the second period, only one branch is evident, with Θ values spread across the entire branch. This indicates no clear relationship between Θ and the tracer, although CO and N_2O maintain a compact positive correlation. In the third period, nearly all data points are confined to a small region of correlation space, while potential temperature varies strongly within this region. These features suggest that the air masses were affected by a process that disrupted the relationship between CO, N_2O, and Θ, with mixing being a likely candidate. Notably, the first and third periods show signatures of recent mixing, coinciding with indications of recent turbulence in the ERA5 analysis (Fig. 2b). In contrast, the second period more closely resembles the background CO–N_2O relationship. This may indicate that the air masses during the first and third periods experienced more recent local mixing, whereas the air mass observed in between had been mixed earlier and was closer to equilibrium.

An analysis of power spectral densities of w, Θ (Fig. 4a, b) and N_2O, CO (Fig. 4c, d) also suggests the presence of small–scale turbulent processes. All spectra rather have a slope of -5/3 which is often seen as an indication for turbulence occurrence on the mesoscale and below (e.g., Zhang et al., 2015a; Dörnbrack et al., 2022; Lachnitt et al., 2023). While , the w spectra shows a slope of -3 for the smaller wavelengths, it follows more the slope of -5/3 for frequencies smaller than 0.8 Hz, which is similar to the report of Lachnitt et al. (2023). For higher frequencies (shorter wavelengths), the increase of power spectra to 0.5 Hz could be an indication of turbulent processes below the synoptic scale. Overall, the w and Θ spectra follow the slope close to $k = -5/3$ and can be related to three dimensional isotropic turbulence, which is an indication of dynamic processes on or

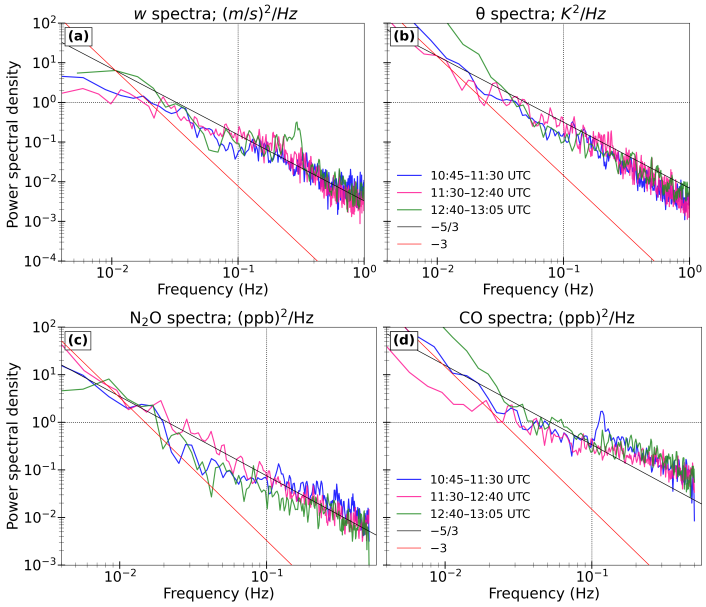


Figure 4. Power spectral densities of (a) measured vertical velocity (in $(\mathrm{m\,s^{-1}})^2$/Hz) and (b) observed potential temperature (in $\mathrm{K^2}$/Hz) from BAHAMAS, and of (c) N_2O (in $(\mathrm{ppbv})^2$/Hz) and (d) CO (in $(\mathrm{ppbv})^2$/Hz) from UMAQS during WISE RF05 for the time periods 10:45–11:30 UTC (blue lines), 11:30–12:40 UTC (red lines) and 12:40–13:15 UTC (green lines). The orange line indicates the slope of -3 (geostrophic turbulence), the thin black line a slope of -5/3 (mesoscale turbulence).

below the mesoscale affecting the flow. Moreover, spectra of N_2O and CO also have a slope close to -5/3 for intermediate frequencies i.e., for smaller wavelengths. From 10^{-2} Hz onward to larger scales, the N_2O spectra follow a -5/3 slope which suggests that small-scale processes, potentially those related to GWs, contribute to turbulent mixing in the lower stratosphere. The question on how much GW contribute to the mixing of these air masses is difficult to answer based on the observations along the flight path. Before we broaden our scope in the analysis to the synoptic scale, we attempt to provide further observational evidence for the presence of GWs in the observations. The close spacings of the measurements shown in Fig. 2 allows the detailed mesoscale structures of the jet/front to be elucidated, including low *Ri*, and possible coherent phase structures of GWs. Nonetheless, the (time interval) resolution of in situ measurements is too large to properly sample waves with horizontal wavelengths of $\sim$100 km in hourly model output data. However, the aircraft flew high enough to identify coherent phase lines and/or mixing lines in the lower stratosphere such as those observed in Fig. 3.

To isolate wind perturbations associated with GWs from the background wind, horizontal wind components (u, v) along the flight track were bandpass filtered using a 4^{th} order Butterworth filter. The filter was applied to remove both large–scale trends and high-frequency noise, retaining signals within a 2–10 minute period range. The resulting perturbations (u', v') were then used to construct hodographs and to assess wave properties from the in situ measurements. These perturbation time series are shown in Fig. A4. Note that, due to distinct sampling frequency and noise characteristics in the measurements, the flight

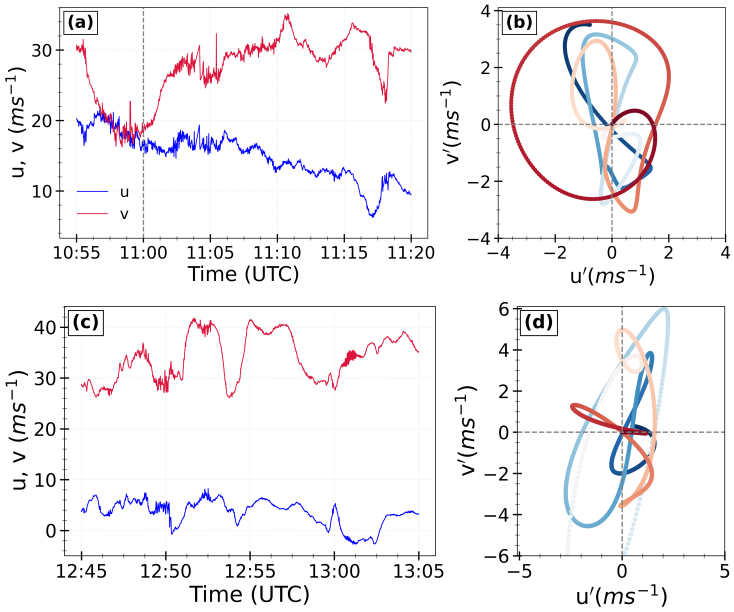


Figure 5. Time series (a, c) of zonal (u, in m s^{-1}; blue) and meridional (v, in m s^{-1}; red) wind component measured during WISE RF05 zoom in for time 10:55-11:20 UTC and 12:45-13:05 UTC. Perturbation hodographs for the corresponding flight period are shown in panels (c) and (d), with trajectories starting in red and ending in blue.

data is filtered using a 4^{th} order Butterworth bandpass filter (Butterworth, 1930), while the model data is processed using the Helmholtz decomposition approach described in Sect. 2.5, in order to isolate GW related perturbations.

Linear theory of GWs in a uniform background flow predicts that one vertical wavelength of an inertia GW traces an elliptical perturbation hodograph (as described in Guest et al., 2000; Plougonven et al., 2003; Yoshida et al., 2024), which rotates anticyclonically for an upward propagating wave, and cyclonically for a downward propagating wave. This technique has some limitations in terms of conditions with strong background wind shear and hence is only suitable for a part of the wave spectrum with low-frequency, long-wave limit (for more details see Plougonven et al., 2003). These hodographs are typically drawn from vertical profiles at a given time. However, due to the limited number of altitude levels available in our dataset, we instead construct a single hodograph using profiles at multiple times at one flight altitude (e.g., as in Gomes et al., 2025). As an example, we use the time series of u', v' at ∼12.5 km flight altitude for the period of high vertical shear and low Richardson number (Fig. 5). The respective time series of u, v is shown in Fig. 5a, c (see also Fig. A4). Both these time periods include multiple ellipses and only few segments show clear evidence of anticyclonically rotating hodographs, i.e., those line segments colored in red in Fig. 5b, d. A well-defined elliptical pattern is evident in Fig. 5b, indicating the presence of upward-propagating GWs. In contrast, although wave-like oscillations are more prominently observed during 12:45–13:05 UTC (Fig. A4), such a coherent elliptical structure is less apparent in Fig. 5d.

As a first summary, we can conclude that a turbulent region has been crossed during RF05. This region shows enhanced vertical shear, low Richardson numbers and signs of tracer mixing. Since there are also signs of GW in the respective time periods, this motivates us to go on with our analysis on how GWs might contribute to this mixing event. For this we will broaden our scope and analyse the larger synoptic situation.

4 Co-occurrence of gravity waves and turbulence in ERA5

In this section, we use ERA5 reanalysis data to investigate potential signatures of GW-induced shear and turbulence. We first examine whether GWs were present over the North Atlantic during the case study period discussed in Sect. 3.3. Subsequently, we explore the relationship between these GWs, vertical wind shear, and turbulence diagnostics in the LMS. Our analysis focuses on the region encompassing the entire flight, defined by 50°N–72°N and 5°W–30°W. The analysis domain is outlined in blue in Fig. 1.

4.1 Analysis of gravity waves and vertical shear

We begin by analyzing the horizontal divergence field to identify location and characteristics of potential GW signatures in the lowermost stratosphere. We define the extratropical tropopause based on the dynamical tropopause definition with a potential vorticity value of 3.5 PVU (1 PVU=1×10^{-6} K m^2 kg^{-1} s^{-1}).

Figure 6a-c shows the horizontal divergence at 12.5 km altitude ($\sim$ 200 hPa) between 11:00 and 13:00 UTC. Alternating divergence and convergence patterns in the horizontal divergence field, indicative of gravity wave activity, are evident near the jet streak exit region, with enhanced signatures between 60°N and 72°N above the Icelandic highlands along the flight track (Fig. 6a). These GWs are likely generated by the interaction of the baroclinic flow with Iceland's topography. These signatures of GWs are persistent over the following hours around Iceland (Fig. 6b, c) and are also evident in the PV field. Horizontal wavelength of these waves is on the order of a few hundred kilometers, similar to typical wavelengths of inertia GWs. On the larger scale, however, all time steps exhibit similar divergence patterns with slight changes in both amplitude and orientation, reflecting a systematic evolution of the wave field.

The corresponding vertical cross section of horizontal divergence at 14.05° W, representing the approximate flight location at 11:00 UTC (marked by the dashed line), is shown in Fig. 6g. The GW propagate clearly upward and change their wavelength in the lowermost stratosphere. While it seems that the GW is rather localized above Iceland in the troposphere, it starts to propagate away from its source in the stratosphere. At this cross section the GW is evident up to about an altitude of 17.5 km. Inspection at later times shows that signal is quite persistent with minor changes in the wave signatures near 14.05° W (see also Fig. B1). It is further notably that ERA5 despite its lower horizontal resolution, is able to capture the appearance of GWs in the LMS. This is consistent with findings of previous studies which analyzed GWs in ECMWF products and reanalyses (e.g., Jewtoukoff et al., 2015, and references therein).

Horizontally propagating GWs with large horizontal wavelengths tend to dominate the horizontal derivatives of momentum fluxes, whereas, upward-propagating large-amplitude GWs can carry substantial momentum vertically across the tropopause.

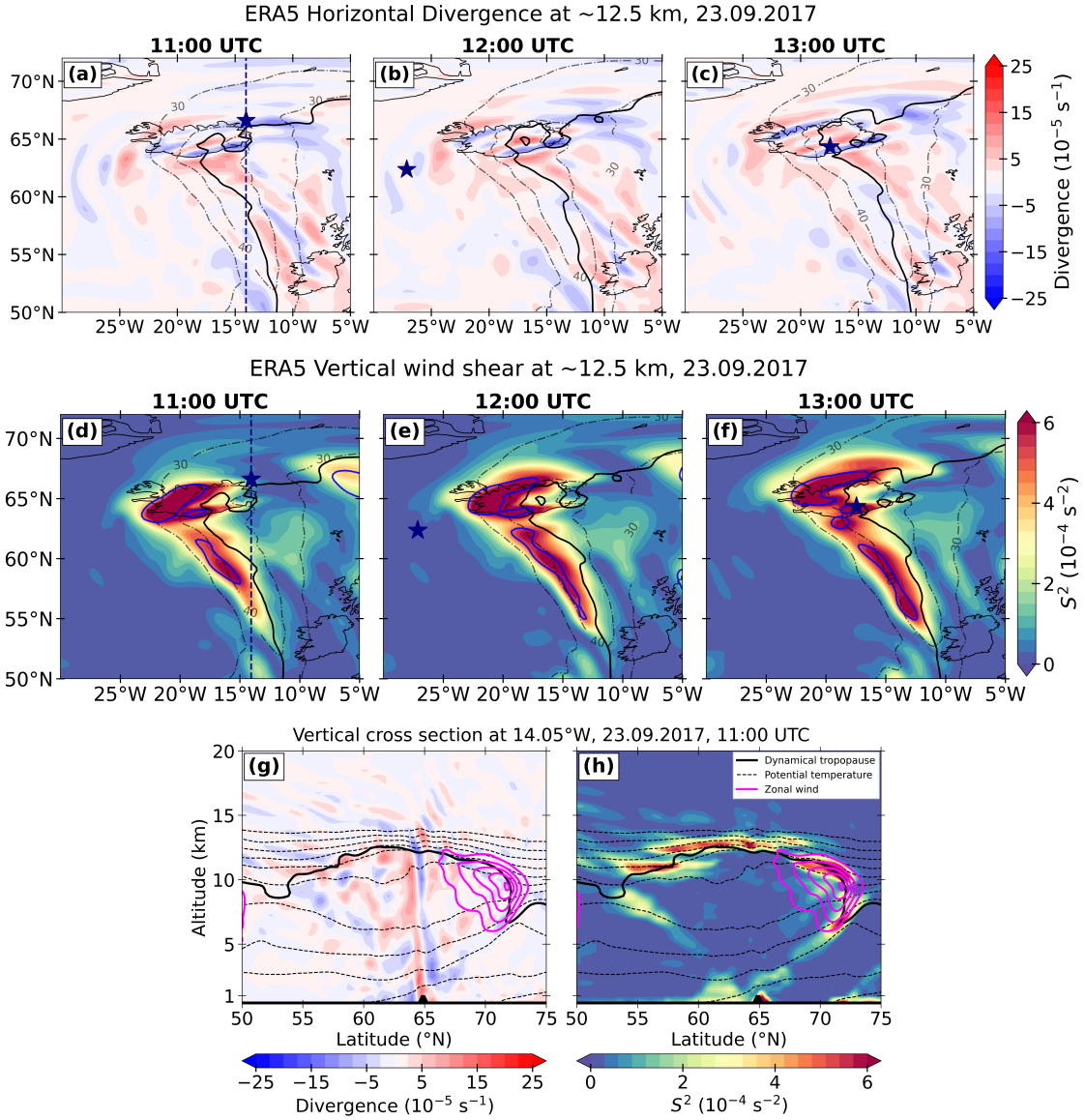


Figure 6. Distribution of horizontal divergence (upper panel) and vertical wind shear (middle panel) at ∼12.5 km altitude for ERA5 reanalysis data at 11:00 UTC (a, d), 12:00 UTC (b, e) and 13:00 UTC (c, f). The dashed lines in upper and middle panels represent corresponding horizontal wind speed for values greater than 30 m s^{-1}. The RF05 flight location during the time shown by blue star. The vertical cross sections of divergence (g) and shear (h) at 14.05° W during 11:00 UTC is shown in lower panel. The solid black line represent the 3.5 PVU as a dynamical tropopause whereas dotted lines in lower panel represent the potential temperature starting from 280 K (bottom) to 380 K (top) with 10 K increments. Magenta contours in (g, h) denote zonal wind speed (20, 30, 40, 50) in m s^{-1} and solid blue lines in middle panel represent $Ri = 1$.

This further modulates the vertical gradients of the wind components across the tropopause, which in turn, leads to higher shear values and with this turbulence occurrence in this region. In the region of the enhanced gravity wave activity we also find a large areas of enhanced vertical wind shear around 12.5 km altitude between 11:00 UTC and 13:00 UTC. There are clear signs of the enhanced shear along the jet-stream south of Iceland. The strongest shear occurs over Iceland in the region of the GW (Fig. 6d-f). Additionally, the regions of enhanced vertical shear show widespread occurrence of reduced Ri values (blue lines in Fig. 6d-f), suggesting a potential for the occurrence of dynamic instability.

Furthermore, the vertical distribution of vertical shear at 14.05° W (Fig. 6h) shows two different regions of enhancement. Large values of the shear are evident in the LMS around the jetstream roughly around 70° N. Additionally, maxima in shear appear further south also in the region of the GW. Since these maxima occur away from the jetstream this indicate that other, potentially smaller–scale features produce the large shear values. Also, there is countable co-location of shear on large scale and shear perturbations on smaller scale (see Fig. B2a) with GW patterns across the tropopause (Fig. 6d-f) and thus the shear location related to the phase of GWs modes remain consistent in vertical distribution. Overall, in this case there is a spatiotemporal co-occurrence of GWs and vertical wind shear.

While the co-occurrence of GWs and enhanced vertical wind shear suggests a possible link, the extent to which small-scale GWs contribute to shear modification across the tropopause remains to be assessed. One possible explanation for this is that vertically propagating, large amplitude, high vertical (short horizontal) wavelength GWs locally modulate the N^2 in the LMS (Kunkel et al., 2014; Kaluza et al., 2019; Zhang et al., 2019), which in turn also allows to accumulate vertical shear in this region. This suggests that GWs may contribute (or influence) partially to the vertical shear generation in the lower stratosphere. On the other hand, the maximum shear in locations other than GW activity, likely generated from the large–scale components including the jet stream or baroclinic disturbance. This further motivates a deeper look at the significance of small–scale GWs to high wind shear, and subsequently to the potential turbulence occurrence.

4.2 Turbulence diagnostics in the LMS

After showing the link between GWs and vertical shear of the total wind field, we move on to a more in-depth analysis of turbulence occurrence. Note again that turbulence occurrence is assessed with predictors derived from the resolved model quantities. For this we analyze the AMF, the vertical wind shear perturbations in the region covered by the flight track over the North Atlantic, i.e., between 50° N–72° N and 5° W–30° W (see blue box in Fig. 1). We focus on the LMS and further limit our analysis to regions with gradient Richardson numbers between 0 and 1. The shear perturbations, $S^{2'}$, show how much shear is related to the small–scale wind perturbations, while the AMF is used to quantify momentum transport due to GWs. One would expect momentum-flux deposition by GWs in the region where GW-induced instability and turbulence occur (Fritts and Alexander, 2003). We also note here that turbulence is a relatively rare event under general atmospheric condition (Sharman et al., 2012; Dörnbrack et al., 2022) and only a few data points are anticipated during episodes of potential turbulence in the LMS.

With this knowledge we create two-dimensional probability density distribution of AMF and vertical shear perturbations in the LMS for $0 \leq Ri \leq 1$ (Fig. 7). We can see that the majority of the points has rather low vertical shear, given by the distribution

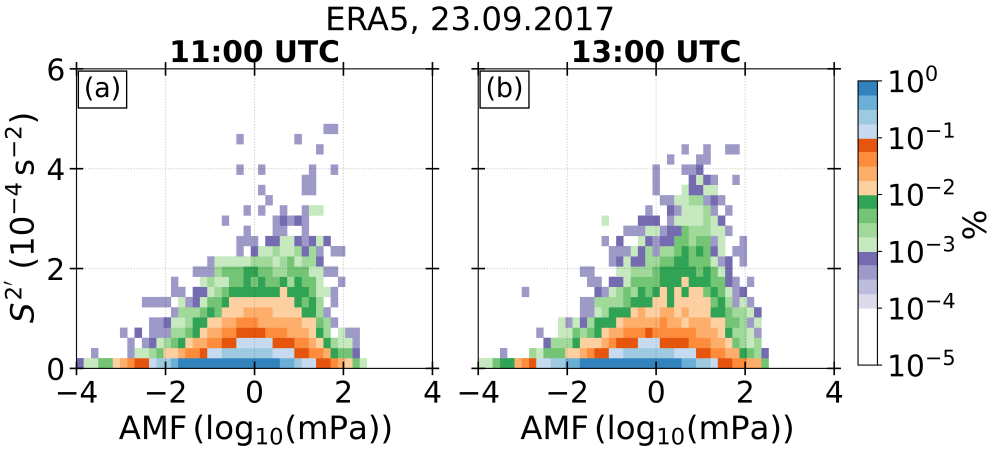


Figure 7. Relative occurrence frequency distribution of absolute momentum flux due to GWs-vertical shear perturbations pair in the LMS for $0 \leq Ri \leq 1$ for ERA5 reanalysis data at 11:00 UTC (a) and 13:00 UTC (b). Normalized counts of PDF distribution is shown. Logarithmic occurrence frequency color scale is applied.

and color code in the figure. However, those regions with the larger vertical shear values ($> 3 \times 10^{-4}\,\mathrm{s}^{-2}$) exhibit also a larger AMF. From this we follow that there is a positive correlation between $S^{2'}$ and AMF in the LMS and the small–scales play a role for the potential turbulence occurrence. We see that this behavior is again quite persistent and especially evident for the time steps of interest of our analysis (see Fig. Fig. 7a, b for 11:00 UTC and 13:00 UTC). Slight changes in the probability density distributions are evident and are most likely related to the evolving flow situation. However, the distributions show a striking similarity to those reported from idealized baroclinic wave experiments (Umbarkar and Kunkel, 2025). Thus, we interpret this co-occurrences of enhanced vertical shear perturbations and AMF as an indication that small-scale dynamics, and especially GWs, contribute to the turbulence occurrence in our case study. The fact that this relation is evident in the idealized experiments further suggests that this is behavior might be rather a general feature associated with baroclinic waves than being a special feature of our case study here.

4.3 Are these GWs responsible for CAT occurrence?

In a next step we turn to the relation between GWs and clear air turbulence. One previously suggested consequence of dynamic instability is that associated inertia GWs may generate CAT when they break (Knox, 1997). In light of this Thompson and Schultz (2021) showed that the emission of inertia GWs, following the release of dynamic instability, instigate light–moderate occurrences of CAT around the unstable region using idealized model simulations. We follow this line of thought and use the turbulent indices, TI1 and TI2, to identify regions of CAT occurrence in our region of interest in the LMS over the North Atlantic (Fig. 8). In contrast with the shear analysis from the previous sections, CAT develops rather in sporadic pockets. Sharman et al. (2006) suggested that these smaller–scale turbulent regions persist for a few minutes around the periphery of the unstable regions. We see similar patterns in our case. It is noteworthy to mention that the turbulent indices are small in the low

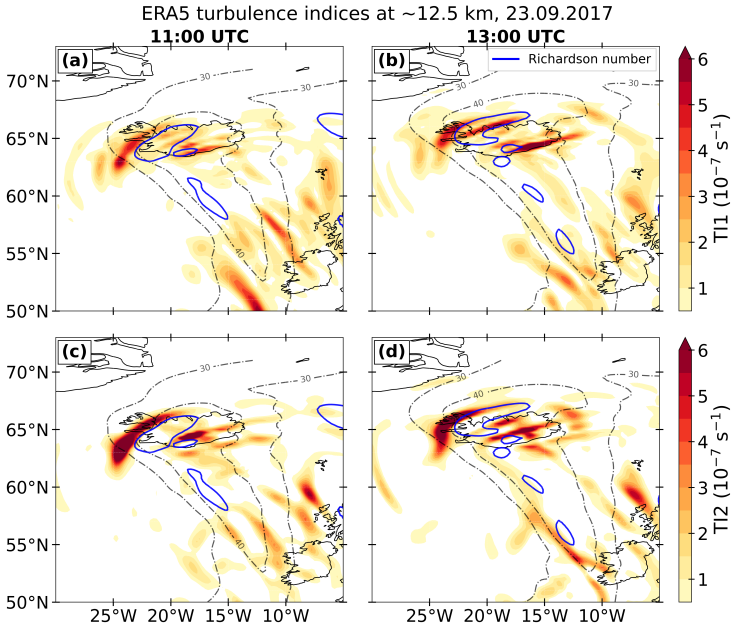


Figure 8. Distribution of turbulent indices TI1 (a, b) and TI2 (c, d) at ~12.5 km altitude for ERA5 reanalysis data at 11:00 UTC and 13:00 UTC. The dashed black lines presents the horizontal wind speed >30 $\mathrm{m\,s^{-1}}$ and blue contours denote $Ri \leq 1$.

gradient Richardson number region south of Iceland but show their largest values over Iceland where Ri is also small. The TI2 also shows generally higher values over Iceland than the $TI1$ which is related to the CVG term in TI2. This and the fact that the CAT indices are generally largest in the areas of GW occurrences suggest that GWs play a crucial role in the turbulence formation, despite the limit of only a hourly temporal resolution of the ERA5 reanalysis data. The picture becomes clearer that GWs while propagating upwards through the tropopause region can increase the vertical shear and thus contribute to the formation of a dynamic instability as well as to the occurrence of CAT.

We calculate the TI1 and TI2 as proxies for CAT from zonal and meridional wind perturbations (u', v'). Since we find several regions where CAT develops simultaneously across the tropopause, we also want to use these indices to quantify the strength of the CAT events based on the ERA5 data. For this we categorize the CAT values into intensity levels as given in Lee et al. (2019, 2022). Light-moderate CAT intensity is then determined by the 95th percentile value of the total occurrences of each index in the LMS. In our case we determine the corresponding threshold values for TI1 and TI2 to $1.4 \times 10^{-7}\,\mathrm{s^{-1}}$ and $1.5 \times 10^{-7}\,\mathrm{s^{-1}}$, respectively (see also Appendix C and Fig. C1).

Collating all turbulence occurrence throughout the simulation, we find that most occurrences fall into this light–moderate category, but some occurrences of moderate intensity are also apparent (Fig. C1a). On the other side, the moderate to greater intensity CAT in TI1 with slightly less occurrences are strong in the positive tail of TI2 (Fig. C1b). Compared to TI1, the TI2 index shows more frequent occurrences of moderate and greater than moderate CAT events (see Fig. C1b), which could again

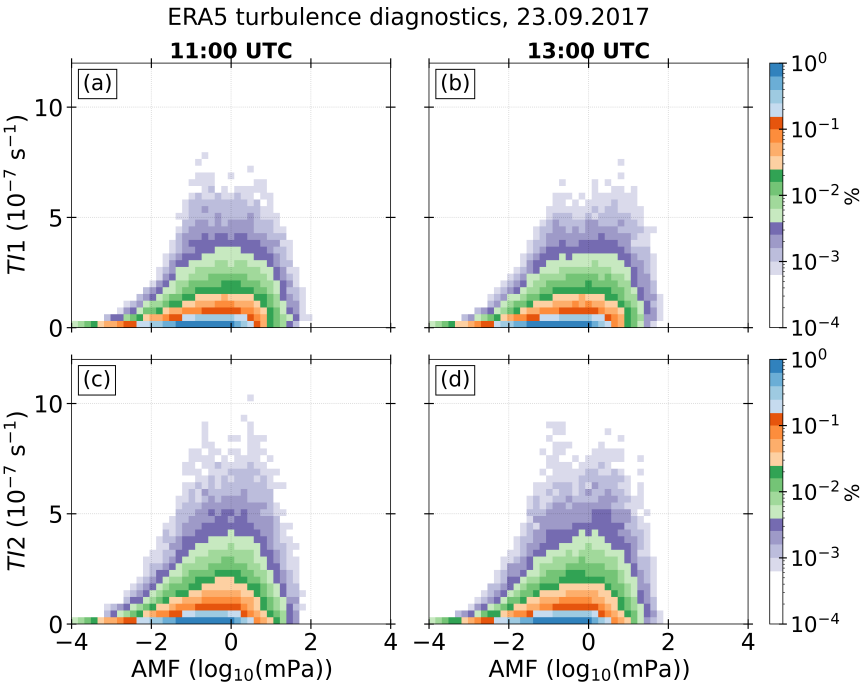


Figure 9. Frequency (%) distribution of absolute momentum flux-turbulent indices TI1 (a, b), TI2 (c, d) in pairs over the LMS for ERA5 reanalysis data at 11:00 UTC and 13:00 UTC. Normalized counts of PDF distribution is shown. Logarithmic occurrence frequency color scale is applied.

be attributed to the additional convergence term in TI2 and thus potentially be a hint that GWs play a substantial role in the formation of strong CAT events.

Similar to the vertical shear perturbations, we finally want to determine the relation between the CAT indices and the AMF. Figure 9 shows the 2D probability distribution of TI1 and TI2 with AMF at two time steps for the LMS over the North Atlantic domain. The shape of the 2D distributions is quite similar to the distribution for the vertical wind shear perturbations. The distributions are tilted towards high CAT indices and high AMF values with only minor changes in time (compare panels (a) and (b) as well as (c) and (d) in Fig. 9). Again the slightly higher occurrences of enhanced TI2 values over TI1 values is evident. Based on these distributions we suggest that the small scales, and again particularly the GWs, do not only enhance shear, which per se is only a prerequisite for turbulence occurrence, but also play a vital role in the occurrence of CAT. Furthermore, this hints towards the important role of the small-scales towards the transport and deposition of momentum in the tropopause region with potential consequences on the distributions of trace species in this region.

In conclusion, the results obtained in Umbarkar and Kunkel (2025) from the idealized cases are also evident in the "real" world in the ERA5 perspective. As of now, the discussion centred around the role of GWs in the occurrence of strong shear in the LMS, and whether potential turbulence occur in the region of the GW-induced shear in ERA5. In the next section, discussion

focuses on sensitivity analysis, that is a comparison for an ECMWF product with finer horizontal grid resolution. Moreover, it is yet to investigate whether this findings are also true in the real world that uses non-hydrostatic dynamical core.

5 Sensitivity analysis: gravity waves and turbulence occurrences in IFS and ICON

The ERA5 analysis suggests that GWs may contribute to the generation of vertical shear and potential turbulence through dynamical processes. In this section, we investigate how GW signatures change with increasing horizontal resolution and how their occurrence, location, and characteristics depend on horizontal grid spacing in the UTLS. From here onward, we focus on the 11:00 UTC time step, as the analysis at 13:00 UTC leads to the same conclusions regarding the role of GWs in generating shear and potential turbulence.

5.1 Analysis of GW, shear and turbulence in the IFS

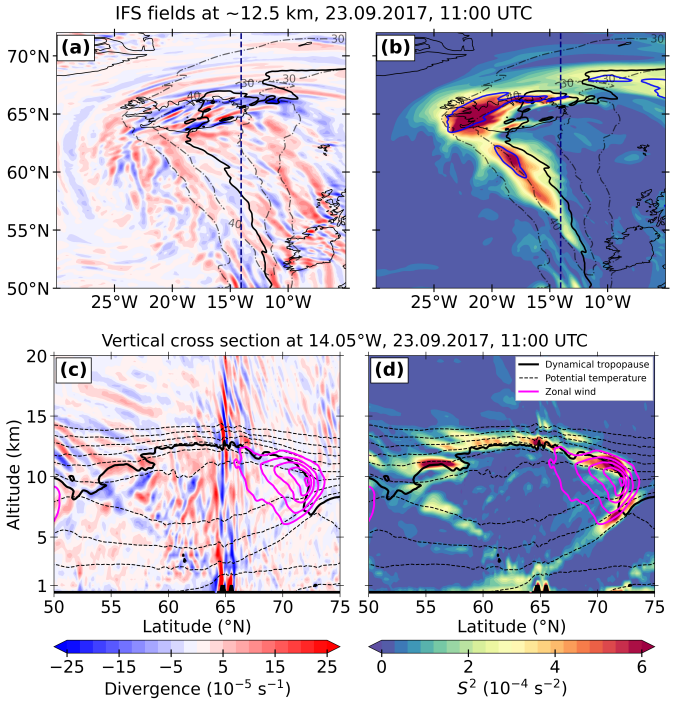


Figure 10. Distribution of horizontal divergence (a) and vertical wind shear (b) at ∼12.5 km altitude for IFS data at 11:00 UTC. The dashed lines in upper and middle panels represent corresponding horizontal wind speed for values greater than 30 m s^{-1}. The RF05 flight location during the time shown by blue star. The vertical cross sections of divergence (c) and shear (d) at 14.05° W during 11:00 UTC is shown in bottom panel. The solid black line represent the 3.5 PVU as a dynamical tropopause whereas dotted lines in lower panel represent the potential temperature starting from 280 K (bottom) to 380 K (top) with 10 K increments. Magenta contours in (g, h) denote zonal wind speed (20, 30, 40, 50) in m s^{-1} and solid blue lines in (c) represent the $Ri = 1$.

We first investigate the sensitivity of the results to horizontal resolution using IFS forecasts with a finer spatial resolution than ERA5. At synoptic scales, the flow evolution closely resembles that derived from ERA5 and discussed in Sect. 4.1. However, slight deviations are evident at meso scales as well as in the location of GW structures (Fig. 10). These similarities and differences are highlighted in Fig. 10a, where IFS captures finer horizontal structures of divergence, indicative of GWs activity covering Iceland with moderate amplitudes in the northwestern sector, rather with larger amplitude small–scale features. The corresponding vertical distribution at 14.05° W shows a packet of GW propagating upward into the lower stratosphere, with a relatively larger vertical wavelength (∼2-3 km) and short horizontal (∼100 km) wavelength (Fig. 10c). As expected, this reveals the presence of finer-scale structures in IFS compared to ERA5 (see also Fig. 6g). This indicates that GW characteristics, especially their horizontal structure, are strongly dependent on spatial resolution. This dependence arises not only from the changed grid spacing but also to the representation of orography, as higher horizontal resolution better resolves terrain features and can therefore generate smaller-scale orographic GWs. Overall, these results suggest that the horizontal resolution largely controls the magnitude of the GW fluctuations in both reanalyses and forecasts.

Further analysis of vertical shear (Fig. 10b) at the same altitude reveals high shear values around 60–65° N over the Iceland, especially in the proximity of the observed GWs. The large vertical shear values are accompanied by low Richardson numbers, especially over Iceland (blue line in Fig. 10b highlights $Ri \leq 1$). This pictures resembles the situation described in ERA5, with a co-occurrence of GWs, enhanced shear and low *Ri* over Iceland. Further south, we also find a region of enhanced shear and low *Ri* values but no signs of GWs. The turbulence occurrence in this region is therefore rather associated with larger scale dynamics related to the jetstream. In summary, the IFS exhibits similar structures in vertical shear, GWs and turbulent regions as ERA5, but the spatial scale of the maxima is notably smaller in the vicinity of the ridge. Also, in the IFS a more pronounced spatio-temporal co-location between shear and GW patterns is evident than in ERA5.

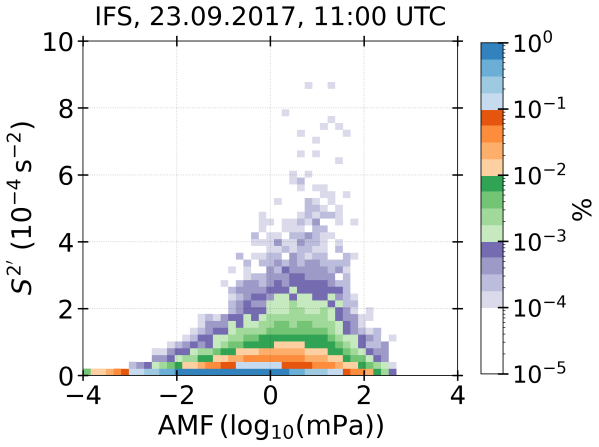


Figure 11. Same as Fig. 7 but for IFS at 11:00 UTC.

Next we look more into the perturbation quantities and start with the occurrence frequency distribution of AMF-vertical shear perturbations for Richardson numbers between 0 and 1 (Figure 11). Since IFS resolves the vertical shear similar to ERA5 and

exhibits a comparable pattern of GWs and S^2, it is not surprising that the positive correlation between AMF and $S^{2'}$ in the LMS is still evident. The most notable difference is that larger values for the shear perturbations are evident in absolute number in the IFS data and also the number of large shear perturbations is increased compared to ERA5 (see Figure 7). The AMF also shows slightly larger values hinting towards a slightly stronger GW activity. Thus, the higher resolved data further support and strengthen our hypothesis that the small scales play are a vital contributor to the occurrence of enhanced shear and further to the occurrence of turbulence in the LMS.

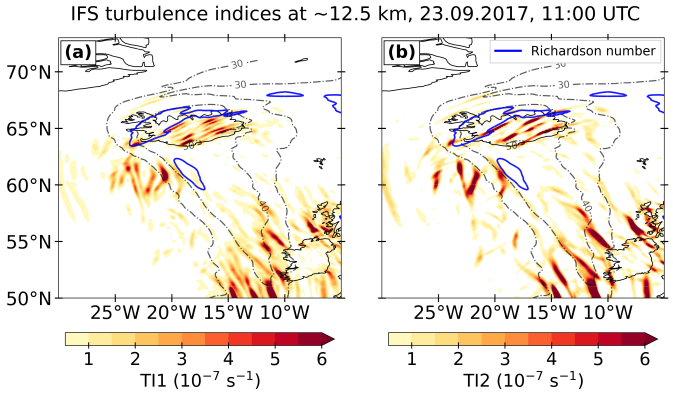


Figure 12. Distribution of turbulent indices TI1 (a) and TI2 (b) at ~12.5 km altitude for IFS. The dashed black lines presents the horizontal wind speed $> 30\,\mathrm{m\,s^{-1}}$ and blue contours denote $Ri = 1$.

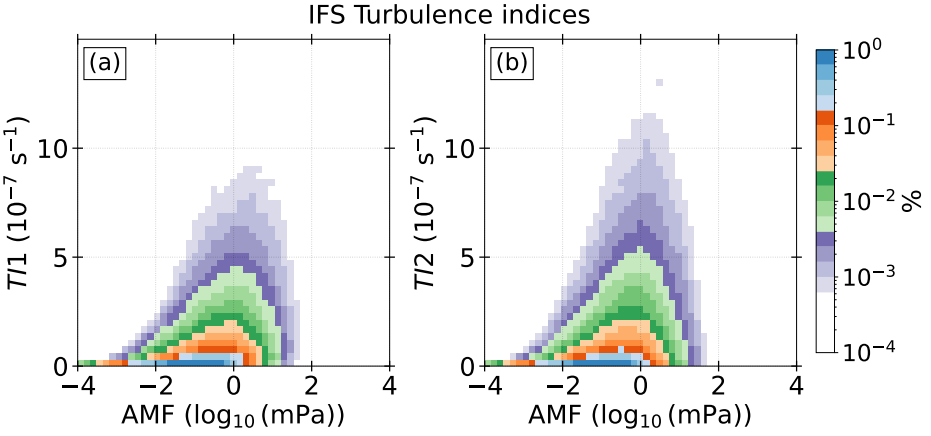


Figure 13. Frequency (%) distribution of absolute momentum flux-turbulent indices TI1 (a), TI2 (b) in pairs over the LMS for IFS data. Normalized counts of PDF distribution is shown. Logarithmic occurrence frequency color scale is applied.

With the apparently stronger shear and GW occurrence in the IFS forecast compared to ERA5, the next question is whether this contributes also to more potential turbulence occurrence. For this we analyze the occurrences of TI1 and TI2 and start with the horizontal distributions of these turbulent indices (Fig. 12). As before the general structure is quite similar to what

has been observed in ERA5 (see Figure 8) but the patches of enhanced TI1 and TI2 are more localized in the IFS. TI1 and TI2 show only little differences in the IFS in their spatial occurrence, the TI2 exhibits slightly larger values. Interestingly, regions of low Richardson number marked by the blue line hardly overlap with enhanced turbulence markers. As before we can determine the threshold value for light moderate CAT with the 95th percentile criterion. The threshold values for TI1 and TI2 are then $2.1 \times 10^{-7} s^{-1}$ and $2.45 \times 10^{-7} s^{-1}$, respectively (Fig. C1). Both these values are remarkably above the threshold values for ERA5, highlighting again that the IFS shows clearer signs of potential turbulence occurrence. This is also the case in the entire LMS as is evident from two-dimensional occurrence frequency distributions of TI1-AMF and TI2-AMF pairs (Fig. 13). Compared to the distributions from ERA5, the slightly higher maximum values for TI1 and TI2 are clearly recognizable. However, almost more striking is the fact that the distributions generally show more high occurrences of these indices and thus more potential turbulence occurrence in the LMS. Both distributions are skewed towards high AMF and high turbulence indices and as such support the hypothesis that turbulence occurs most intense when the AMF is large.

So far, this section has focused on the role of GWs in generating strong shear in the LMS and on whether clear-air turbulence occurs within regions of GW-induced shear in ECMWF datasets, which employ a hydrostatic dynamical core together with semi-implicit and semi-Lagrangian numerical schemes. We now investigate whether these findings also hold in ICON simulations of the same case. This provides a unique opportunity to examine the event across three model domains (with and without convective parameterization) and to relate the results to our previous idealized ICON simulations (Umbarkar and Kunkel, 2025).

5.2 Analysis of GW, shear and turbulence in the ICON

In this section we will not only analyze the differences between the ICON model as an model using a non-hydrostatic approach and the hydrostatic models from ECMWF. We will further see the effects between the ICON from the global instance with 13 km effective grid spacing down to a realization with 3.3 km effective grid spacing. More details about the simulations and physical parametrization schemes used for this simulations are given in Sect. 2.4. We begin by examining the distribution of horizontal divergence at 12.5 km altitude (Fig. 14). Overall, the structure is similar to the ECMWF models (reanalysis and forecast). Pronounced GW activity over the northeastern Icelandic highlands is evident in all domains (Fig. 14a–c), with enhanced wave signatures between 60°N and 72°N, particularly over and east of Iceland along the flight track. The ICON simulation with $\Delta x \approx 3.3$ km captures GW activity throughout the analysis domain, including moderate wave activity in the northwestern sector (Fig. 14c), although it exhibits large-amplitude, small-scale wave features.

Notably, the ICON simulation with $\Delta x \approx 6.5$ km reveals prominent upward-propagating GWs of relatively small amplitude that closely resemble those in the IFS and are not clearly captured in ERA5 (see also Fig. B3). Furthermore, the $\Delta x \approx 13$ km simulation exhibits a vertical structure similar to that of the IFS, with a slightly shorter vertical wavelength of approximately 3 km and wave signatures extending up to about 17.5 km altitude (Fig. B3a). In contrast, the finer-resolution simulation (Fig. B3c) displays larger-amplitude waves with longer vertical wavelengths that propagate upward beyond approximately 19 km altitude. It should be noted that the shallow convection scheme employed in the nested domains ($\Delta x \approx 6.5$ km and $\Delta x \approx 3.3$ km) may contribute to the emergence of additional small-scale wave signatures. All three domain clearly exhibit a more pronounced

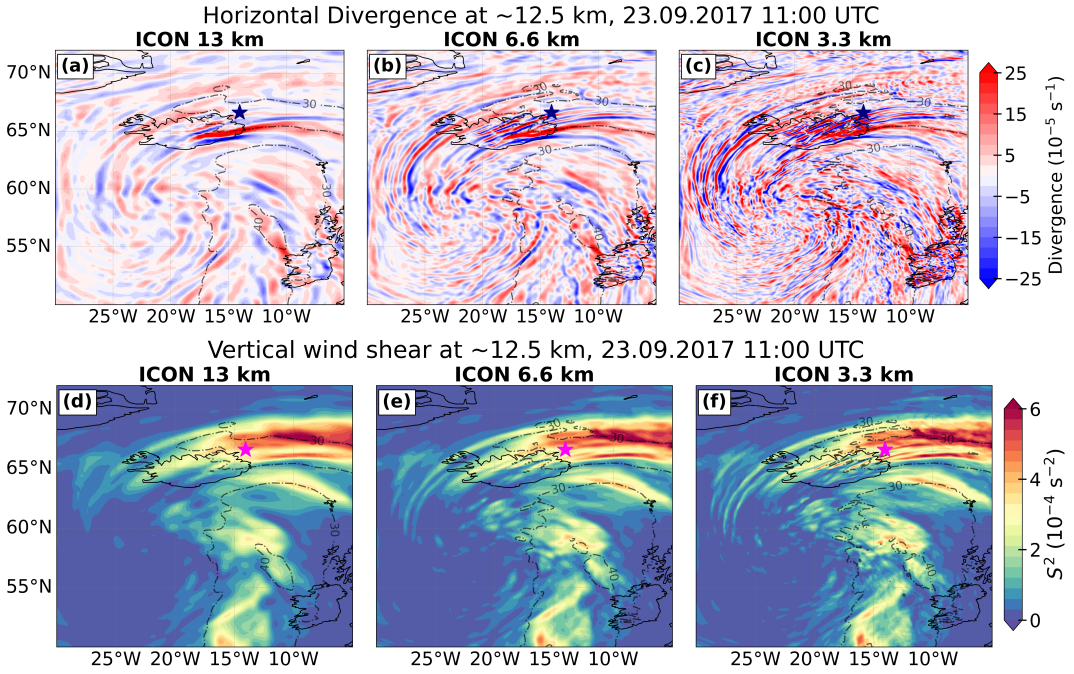


Figure 14. Distribution of horizontal divergence (upper panel) and vertical wind shear (lower panel) at 12.5 km altitude for ICON 13 km, 6.5 km and 3.3 km resolution nested simulations overlaid with flight location at 11:00 UTC shown by star. The dashed line represent corresponding horizontal wind speed for values greater than 30 ms^{-1}.

GW signatures with resolved finer scales, with slight changes evident in both amplitude and magnitude of GWs. Moreover, the appearance and occurrence of GWs as well as small-scale features are highly dependent on the model grid spacing and convection processes implemented therein.

The corresponding horizontal distribution of vertical shear (Fig. 14d–f), shows the maximum shear abundance northeast from the maximum GW signals, north of 65° N and east of 14° W. The three domains show similar structures, in particular, the maximum south of Iceland is weaker in ICON than in the ECMWF models. The ICON simulation with the finest grid spacing shows the highest shear values and generally, the shear becomes more localized and shows banded structures in the regions of strong divergent signals. This hints towards a clear relation between the divergence and the shear in the tropopause region and in the lower stratosphere (see also Fig. B3d-f). A potential reason for the enhanced small–scale divergence in the higher resolution simulations is most likely related to the different representation of convective activity with consequences for the higher shear abundance in the lower stratosphere. Moreover, this overall behaviour indicates that both horizontal and temporal resolution substantially influence the magnitude and representation of GW fluctuations in the forecasts, consistent with the findings presented in Sect. 5.1. This highlights the need to properly simulate GWs and to effectively capture small-scale processes accounting suitable higher spatial resolution.

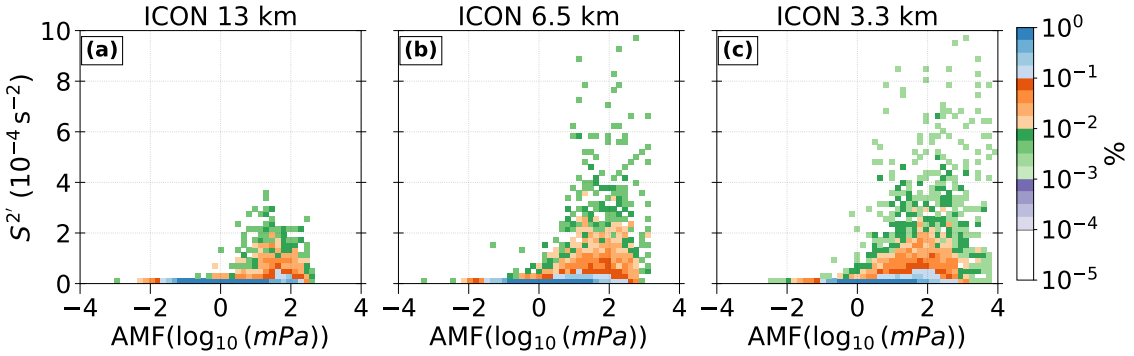


Figure 15. Relative occurrence frequency distribution of absolute momentum flux due to GWs-vertical shear perturbations pair in the LMS for $0 \leq Ri \leq 1$ for ICON 13 km, 6.5 km and 3.3 km resolution nested simulations at 11:00 UTC. Normalized counts of PDFs distribution is shown. Logarithmic occurrence frequency color scale is applied.

We now move on to further investigate the previously identified close relationship between momentum flux and shear perturbations in the context of turbulence occurrence within the LMS. For this, both AMF and $S^{2'}$ quantities are masked for the regions in the LMS where potential turbulence (i.e., $0 \leq Ri \leq 1$) may occur. A closer examination reveals that in general the AMF values have larger values compared to those in the ERA5 and IFS and that enhanced shear occurrences occur also at an order larger than in the ECMWF models (see Fig. 15). It becomes also quite clear that the maximum shear perturbation values increase substantially and that there is a stronger change in the distribution from the simulation with $\Delta x \approx 13$ km to the simulation with $\Delta x \approx 6.5$ km than for the simulations with finer grid spacing. Nevertheless, also in ICON it is the case that the finer the grid, the stronger the shear perturbation and also the stronger the GW activity measured by the AMF.

The fact that the two simulations with the finer grids show similar distributions is interesting, since they differ in the representation of the convection. In the higher resolution simulation, convection is permitted while it is still parameterized in the simulation with $\Delta x \approx 6.5$ km. Nevertheless, the co-relation between AMF and $S^{2'}$ exhibits almost an identical pattern during potential turbulent episodes (see red colors shading in Fig. 15b, c). Thus, while finer resolution leads to a more detailed representation of GWs, the positive association between momentum flux and enhanced shear remains robust across all simulations. This behaviour is consistent with the results presented in Sect. 5.1 and with idealized studies showing that GW-induced perturbations enhance shear, thereby preconditioning the flow for shear-driven instabilities and subsequent potential turbulence generation.

To this point, the results obtained from the analysis of vertical shear, vertical shear perturbation and absolute GW momentum flux give potential for turbulence occurrence. In particular, it could be possible that the identified shear and small-scale structures are primarily associated with the synoptic-scale flow rather than directly linked to (clear-air) turbulence. While the

preceding interpretation relies on the previous studies, this issue can be addressed more directly by examining the relationship between the CAT indices and AMF.

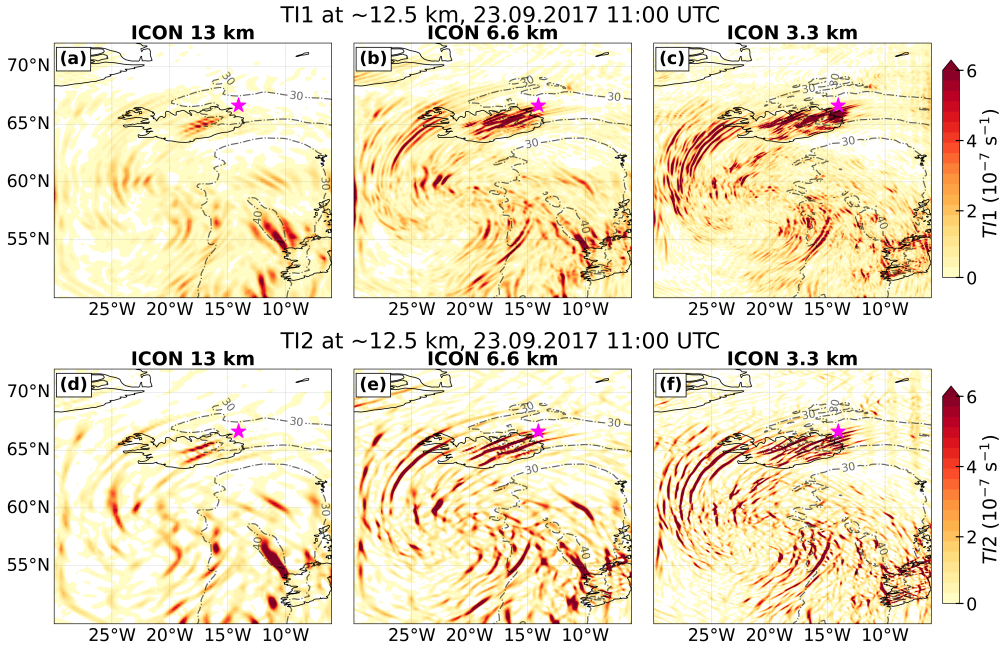


Figure 16. Distribution of turbulence indices TI1 (a-c) and TI2 (d-f) at ~12.5 km altitude for ICON 13 km, 6.5 km and 3.3 km resolution nested simulations. The dashed line represent corresponding horizontal wind speed for values greater than 30 $\mathrm{m\,s^{-1}}$.

Again, we turn to a brief discussion on the turbulence indices TI1 and TI2 calculated on the three ICON domains to assess potential differences between the ICON domains and between ICON and ERA5. For both TI1 and TI2, there are significant changes from the coarse to the fine resolution ICON simulations. While the patterns of TI1 and TI2 emerge in the same locations, the strength and mesoscale structures vary. Banded structures of enhanced TI1 and TI2 emerge over the North Atlantic and over Iceland. These bands carry higher values for the turbulence indices as the resolution becomes finer and become more apparent in the higher resolved domain (Fig. 16). Overall, on synoptic scales turbulence occurrence in all ICON, ERA5 and IFS data sets differ only slightly, while the difference emerge on the mesoscale. Thus, the finer resolved simulations exhibit generally more pockets of enhanced turbulence and often the CAT indices show additionally higher values, which may be directly followed from the fact that more of the GW spectrum is resolved as the resolution becomes finer. Additionally, this seems to directly affect the domain in such a way that more regions show an enhanced potential for potential turbulence occurrence. This is somewhat expected and is also reflected in the relative occurrence frequency of TI1 and TI2 (Fig. 17). The largest TI1 and TI2 values occur in the ICON domain with highest resolution, indicating that potential for more CAT is resolved in this domain. It is particular interesting to see that at smaller TI1 and TI2 values the histograms for the two finer resolved ICON simulations show almost the same relative frequency while they differ substantial for larger values and as

such for stronger turbulence occurrences. Additionally, ICON and IFS show similar relative frequencies of TI1 and TI2 and especially more intense turbulence occurrence on the moderate to moderate or greater CAT category (see also Appendix C).

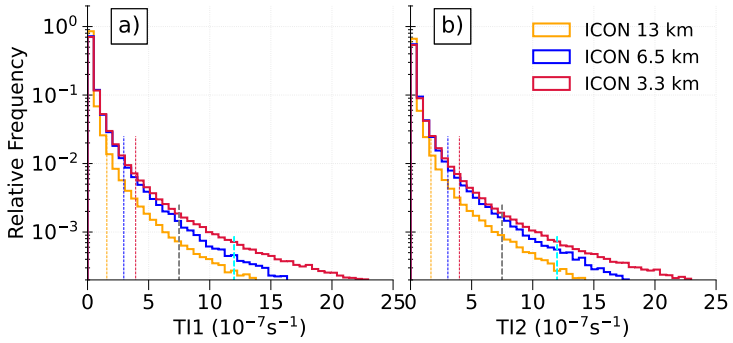


Figure 17. Relative occurrence frequency distribution of (a) TI1 and (b) TI2 for three ICON domains in the LMS. Corresponding to histogram, colored dashed lines indicate threshold retrieved as the 95th percentile over the LMS domain distribution that is considered as threshold for light moderate category. Grey and aqua lines represent the threshold for moderate ($7.5–12 \times 10^{-7}\,s^{-1}$) and moderate to greater ($>12 \times 10^{-7}\,s^{-1}$) intensity CAT, respectively.

The joint histograms of TI1 – AMF and TI2 – AMF pairs in the LMS support the previous findings, in a sense that a positive correlation between turbulence indices and AMF (Fig. 18) is evident across all resolutions. Additionally, the turbulence indices reach higher values in the simulations with finer grid spacing and also the AMF shows a tendency to larger values in the higher resolved simulations. One possible explanation for this could be the strong GW activity that is originated from the convective source in higher resolution experiments. This and the better resolved small–scale dynamical features are most likely responsible for the amplification of shear and turbulence indices. Consequently, highlighting vertically propagating GWs, and GW-induced shear, could then play a significant role not only in the generation of CAT, but also in its dynamics and evolution. This suggests that improved representation of GW-like small-scale structures at higher resolution could give more accurate prediction of such turbulence events.

An interesting observation is the higher occurrence of positive correlations of TI1 – AMF and of TI2 – AMF in ICON compared with Fig. 15, despite ICON exhibiting weaker and more fragmented shear perturbations near regions of low *Ri* than ERA5 (Fig. 7) and IFS (Fig. 11). A plausible explanation is that enhanced local flow deformation during turbulent events in the LMS partly compensates for weaker resolved shear, resulting in a higher occurrence of TI1 within GW-affected regions. Nevertheless, the forecast skill of DEF as a turbulence diagnostic has previously been linked to frontogenesis, enhancement of thermal wind shear (Ellrod and Knapp, 1992), and local GW activity (Kunkel et al., 2014).

Furthermore, results from both the IFS and ICON models support the hypothesis that differences in spatio-temporal resolution sensitivity primarily arise from horizontally propagating GWs with large horizontal wavelengths, which dominate the horizontal gradients of momentum flux. In contrast, large-amplitude upward-propagating GWs mainly contribute to vertical wind

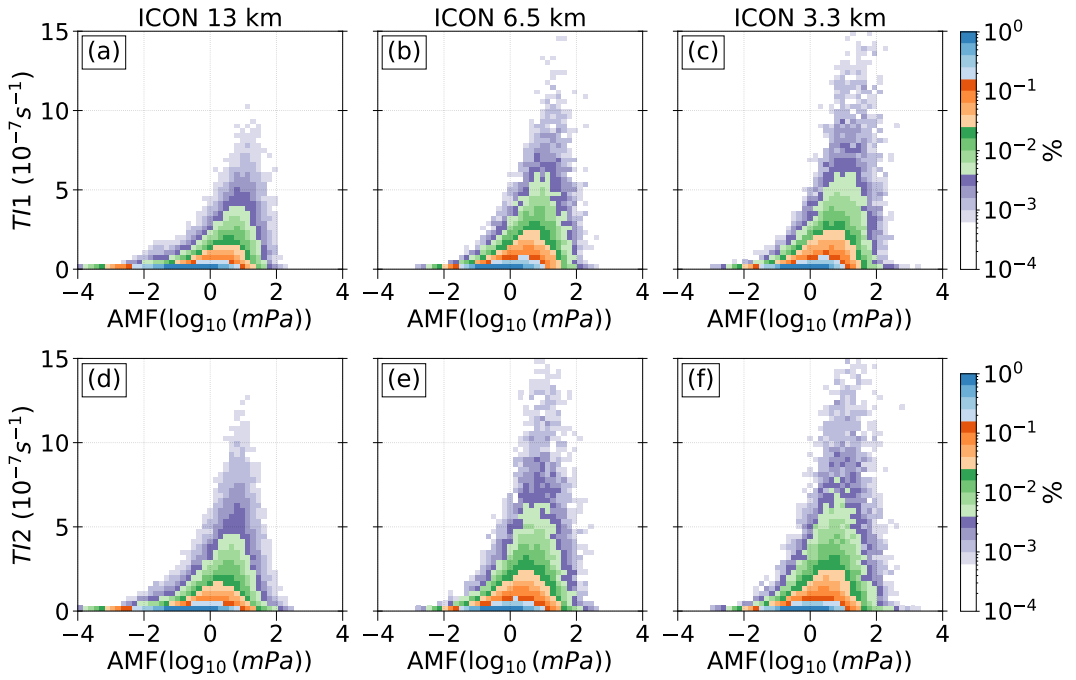


Figure 18. Frequency (%) distribution of absolute momentum flux–turbulent indices TI1 (a-c), TI2 (d-f) in pairs over the LMS for ICON 13 km, 6.5 km and 3.3 km resolution nested simulations at 11:00 UTC. Normalized counts of PDFs distribution is shown. Logarithmic occurrence frequency color scale is applied.

shear through the vertical gradients of the wind components. Together, these effects promote stronger shear, lower Richardson numbers, a greater likelihood of dynamic instability, and consequently higher occurrences of TI1 and TI2 .

6 Turbulence diagnostics in a zonal framework

In this section, we turn our perspective to a more general feature of the LMS which has been described recently in Kaluza et al. (2021, 2022). We first examine the occurrence of the extratropical TSL (Kaluza et al., 2021) across three available datasets: two ECMWF products and a large domain ICON simulation. Afterwards, we investigate the role of GWs in the formation of the TSL and whether turbulence occurs in the region of the TSL. Note here that, we consider ICON simulation with $\Delta x \approx 13$ km, as this is the resolution closer to the ECMWF reanalysis and forecast data. This will allows us to gain a comprehensive view of synoptic-scale structures across the entire extratropical lowermost stratosphere.

We first start with the shear abundance in the extratropics. The TSL has been defined via an exceedance of a defined threshold value of vertical wind shear, i.e., $S^2 \geq S_t^2$ where $S_t^2 = 4 \times 10^{-4} s^{-2}$ (Kaluza et al., 2021). We apply an analogous method to our case study at an instantaneous time step in our limited area over the North Atlantic at which we observed the GW-induced shear enhancement.

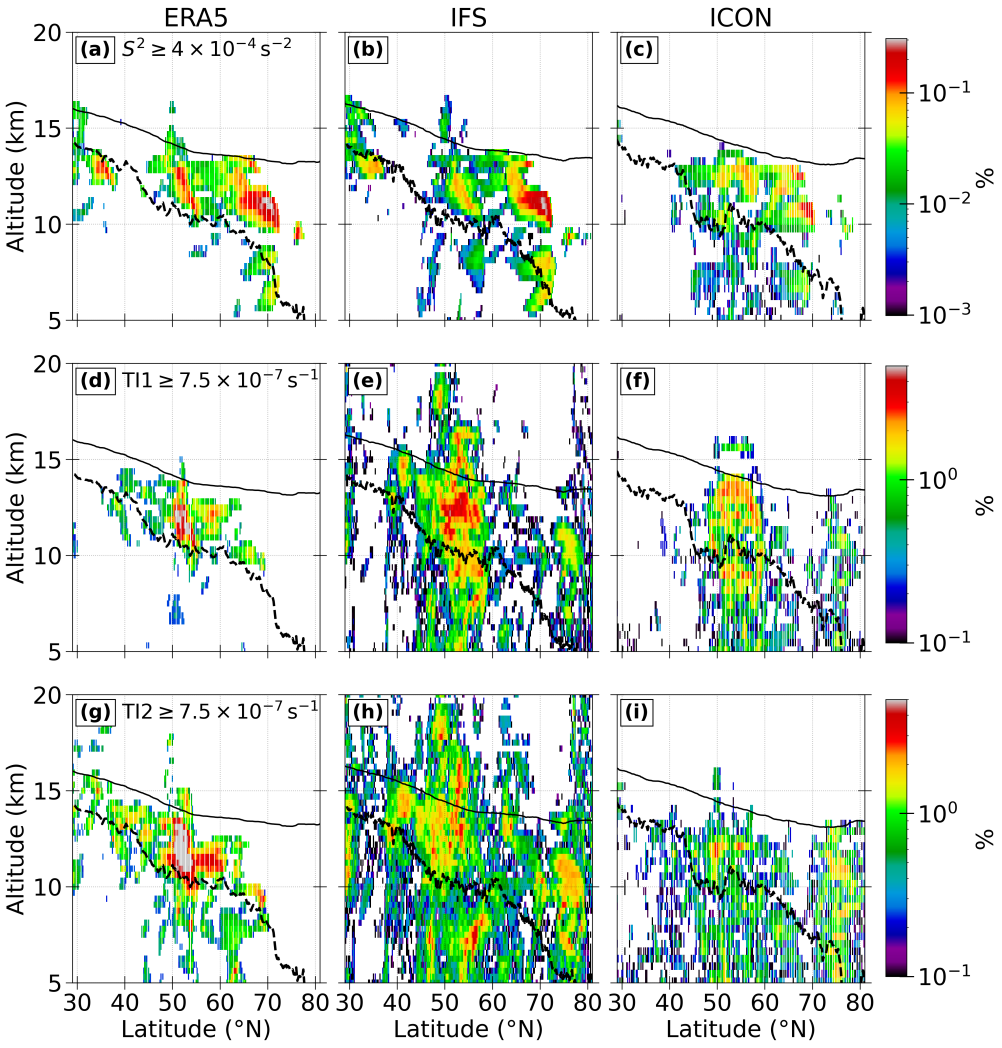


Figure 19. Relative occurrence frequency distribution of grid volumes that exhibit (a-c) $S^2 \geq 4 \times 10^{-4} s^{-2}$, (d-f) TI1 $\geq 7.5 \times 10^{-7} s^{-1}$ and (g-i) TI2 $\geq 7.5 \times 10^{-7} s^{-1}$ over the North Atlantic domain on 23rd September 2017, 11:00 UTC for ERA5, IFS, and ICON. Panels (d–i) represent regions of moderate-intensity CAT occurrence. The occurrence frequencies are shown with logarithmic frequency contours, displaying the data in bins of sizes $\Delta y = 0.2°$ and $\Delta z = 500\,\mathrm{m}$. The zonal-mean dynamical tropopause (3.5 PVU isosurface; black dashed line) and the zonal-mean 380 K isentrope of potential temperature (solid line) are overlaid.

Figure 19a-c shows the relative occurrence frequencies counted in zonal direction for S^2 exceeding the threshold, i.e., $S^2 \geq S_t^2$ in the UTLS. In regions of high tropopause altitudes, shear exceedance are associated with ridges of baroclinic waves and GW activity (e.g., Kaluza et al., 2021; Kunkel et al., 2019, (see also Sect. 4.1)). The pronounced shear occurrences are observed in between 45° N and 60° N in ERA5 and IFS, and with a slightly occurrence in ICON. Overall, this further supports the

results observed in Sect. 4.2 and Sect. 5, where the LMS exhibit the high abundance of shear near Iceland in relation to GW momentum flux.

We further explore the relation to potential turbulence through the zonal occurrence of CAT indices, that means for TI1 and TI2 exceeding the threshold ($\geq 7.5 \times 10^{-7} s^{-1}$), correspond to moderate category CAT occurrences (Fig.19d-i). In the zonally integrated view of TI1, we observed the substantial TI1 occurrences at and farther northward to the highly sheared regions (Fig.19d-f). In ERA5, enhanced frequencies indicate an abundance of moderate level CAT out of total potential CAT occurrences, see the region around 50° N in the LMS. IFS rather shows the pronounced CAT between 45° N and 60° N (Fig. 19e), with wider spread out in TI2 occurrences (Fig. 19h). In contrast to the similarities noted between ICON and IFS in Sect. 5, here ICON exhibits slightly lower occurrences of CAT indices which are rather weaker but broadly distributed in TI2 (Fig. 19f, i). Overall, both TI1 and TI2 exhibit identical pattern in terms of occurrences in the LMS (compare Fig. 19d-f and g-i). Besides this, regions with enhanced shear but absent TI1 occurrences (e.g., near 35° N and 70° N in ERA5 and IFS) point to shear generated by large–scale features such as the jet stream, rather than by GWs. In sum, the turbulence diagnostics reveal turbulence hotspots near typical aircraft cruising altitudes (∼10–13.5 km) in the North Atlantic across all datasets, consistent with the altitude range where strong shear layers frequently occur.

The question remains whether GWs are relevant to the extratropical TSL and, consequently, to CAT hotspots. Shorter GWs, which propagate more vertically, generally carry larger momentum fluxes. If these waves contribute to CAT generation, momentum-flux deposition would be expected in regions where GW-induced turbulence occurs. The largest AMF magnitudes are concentrated in the upper troposphere and extend into the lower stratosphere (Fig. D1). At first glance, regions of enhanced AMF and strong vertical AMF gradients appear to coincide with areas of elevated shear $S^2 \geq S_t^2$ and potential turbulence in the LMS. If GWs play a significant role, one would expect at least a quasi-spatial co-occurrence of enhanced shear, elevated turbulence indices, and increased GW momentum flux.

Figure 20 shows the AMF in shear-dominated regions and areas prone to moderate-intensity CAT. In the vicinity of strong shear, both ERA5 and IFS exhibit enhanced AMF predominantly above the tropopause, particularly at midlatitudes (Fig. 20a,b). Notably, ERA5 displays a pattern similar to that of IFS, despite its lower resolution. In contrast, ICON reveals more localized but substantially stronger AMF maxima near regions of enhanced shear (Fig. 20c). These elevated fluxes indicate enhanced GW activity associated with baroclinic disturbances. Regions of pronounced shear largely coincide with areas of amplified GW activity, supporting the previously identified relationship between GWs and enhanced shear. This spatial overlap further suggests that small-scale processes may contribute significantly to turbulent mixing. This findings further agree with the conclusion of the previous studies of baroclinic life cycles (Kaluza et al., 2019, 2021) and process study (Kunkel et al., 2019; Umbarkar and Kunkel, 2025).

Finally, the relationship between GWs and CAT is assessed using the AMF distribution in the vicinity of TI1 (Fig. 20d–f) and TI2 (Fig. 20g–i). In ERA5, turbulence hotspots largely coincide with enhanced GW activity, with elevated AMF spanning the tropopause and the LMS. IFS exhibits a broader AMF distribution, characterized by strong vertical AMF gradients near elevated TI1 values and a wider spatial extent around TI2 hotspots (Fig. 20e,h). In contrast, ICON reveals more intense small-scale AMF structures and sharper vertical gradients throughout the UTLS, likely associated with resolved GWs (Fig. 20f,i).

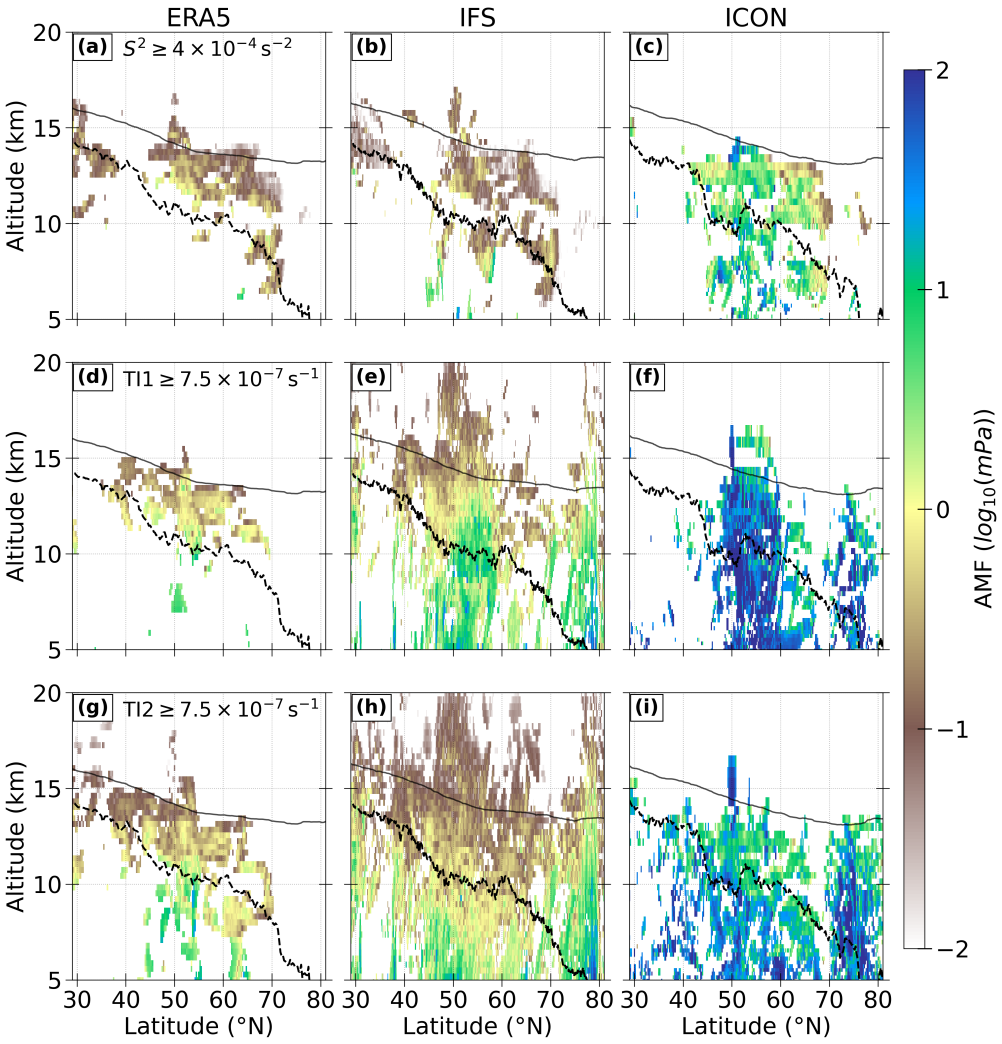


Figure 20. Zonal mean resolved GW absolute momentum flux (AMF, $log_{10}(mPa)$) values conditioned on regions where (a-c) $S^2 \geq S_t^2$, (d-f) TI1 $\geq 7.5 \times 10^{-7} s^{-1}$ and (g-i) TI2 $\geq 7.5 \times 10^{-7} s^{-1}$. All values are vertically binned with $\Delta z = 500\,\mathrm{m}$. The zonal-mean dynamical tropopause (3.5 PVU isosurface; black dashed line) and the zonal-mean 380 K isentrope of potential temperature (solid line) are overlaid.

Overall, enhanced CAT occurrence is generally accompanied by increased vertical AMF gradients. This spatial correspondence suggests that GW activity contributes to the formation of the observed turbulence hotspots.

Besides this, some uncertainty remains in the quantitative assessment of GW momentum fluxes, as the representation of unresolved sources may affect both their magnitude and distribution. An important note is that ICON has been shown to reproduce satellite-derived GW flux patterns without requiring additional parameterizations for unresolved waves over the middle stratosphere (Stephan et al., 2019b). However, Toghraei et al. (2025) suggests that its non-orographic parameterizations may underestimate the dynamical filtering of westward-propagating waves in the mid-latitude region. Nonetheless, the enhanced wave

momentum fluxes co-located with regions of high TI1 occurrence, supports the link between GW activity and CAT generation in the UTLS.

Overall, these findings support the hypothesis that subgrid or small–scale GWs contribute substantially to the enhanced shear formation, the development of high intensity CAT, and hence, consequently could contribute to shaping the ExTL dynamics.

7 Discussion and conclusion

The present study highlights the role of gravity wave induced shear as a key parameter for the tropopause shear layer (TSL, Kaluza et al., 2021) on the basis of observations, reanalysis and forecast data. We note that this is key for the potential occurrence of clear air turbulence, which manifests as highly transient yet frequent mixing processes in the extratropical lowermost stratosphere. As such these processes may play a crucial role in the formation and maintenance of extratropical transition layer, alongside other processes such as convective injection.

Following the results in Umbarkar and Kunkel (2025), we assess whether we can confirm their findings based on idealized model studies in a real world environment over the North Atlantic during an episode of the airborne mission WISE. We use airborne measurements, ERA5 reanalysis, IFS forecast and a comprehensive model forecast dedicated for this case with ICON. Using the combination of these data sets allows us to comprehensively study the relation between vertical shear, gravity waves and turbulence in the lowermost stratosphere. We combine time series analysis, trace species profiles, tracer-tracer correlations and spectral analysis along with a recently explored hybrid approach based on Helmholtz decomposition method (Wei et al., 2022) and come to the following results:

- Airborne observations indicate mixed air masses in regions of enhanced GW activity and vertical shear. We analyzed a WISE campaign flight over the North Atlantic, where tracer–tracer correlations of CO and N_2O revealed mixed air masses. Vertical profiles showed that these air masses were located in the LMS between 345 and 375 K. Further analysis suggests that the mixing was associated with GWs and occurred recently in regions of persistently low Richardson numbers and enhanced vertical wind shear.

- The ERA5 synoptic analysis reveals persistent orographically generated GWs over the Icelandic highlands. Despite its relatively coarse horizontal resolution, ERA5 captures large-amplitude upward-propagating waves that enhance vertical wind gradients and contribute to shear generation.

- The potential role of GWs in generating shear and turbulence in the LMS is identified through the co-occurrence of small-scale momentum flux, enhanced shear, and low Richardson numbers. GW-induced shear, conducive to turbulence, correlates with envelopes of small-scale GWs ($\sim$100 km wavelength) in the LMS exhibiting similar characteristics. Spectral analysis indicates a downscale energy transfer from small-scale GWs that intensifies shear near $\sim$340 K, creating conditions favorable for clear-air turbulence. Consistently, turbulence diagnostics, including *Ri* on larger and TI1, and TI2 on smaller scales, suggest that GW-induced shear promotes CAT occurrence.

- The dynamical situation is similarly represented in ECMWF ERA5 and IFS data. As expected, the higher-resolution IFS reveals more mesoscale structure, while enhanced vertical shear occurs less frequently in ERA5. Nevertheless, ERA5 captures a large part of the GW spectrum and many shear events, making it suitable for long-term analysis of GW-induced shear over the North Atlantic. It is well suited to characterise the large-scale environment and regions favourable for GW activity, but its limited effective resolution constrains the representation of small-scale shear and turbulence.

- The high-resolution ICON simulations reproduced the analyzed large-amplitude GW event over the North Atlantic reasonably well. Application of vertical momentum fluxes and shear perturbations analysis, flow instability as well as turbulent metrics point to multi-scale interactions dominated by upward-propagating large-amplitude GWs with relatively short horizontal but large vertical wavelengths.

- The ICON model data indicate that the analysis of GW occurrence and associated vertical shear strongly benefit from finer grid spacings. GW activity in the tropopause region is enhanced in convection-permitting simulations, while the GW–shear–turbulence relationship remains similar in convection-parametrized experiments. Compared to ECMWF models, ICON exhibits slightly fewer shear events, suggesting either a redistribution of variance due to resolved small-scale GWs or differences in model formulation and setup.

- Differences in GWs and shear between ECMWF products and ICON are less pronounced in the turbulence indices. Diagnosed turbulent regions show banded structures linked to GWs and GW-induced shear, aligned with upper-level fronts and baroclinic activity (Kaluza et al., 2021). ERA5 and IFS indicate widespread dynamical instability, while ICON shows weaker shear perturbations but higher AMF at low Ri. CAT indices reveal moderate-intensity LMS turbulence in ERA5, with IFS and ICON reproducing this pattern at slightly higher intensity. Overall, GWs play a key role in enhancing shear and CAT in the LMS, and ERA5 is suitable for long-term North Atlantic studies due to its ability to capture GW spectra and their turbulent impact.

The relation between small–scale GW momentum flux has long been used as a reliable index for GW analysis (Plougonven et al., 2003, 2017; Lachnitt et al., 2023; Umbarkar and Kunkel, 2025), hinting towards the possibility for the active role of GWs in producing shear hotspots along with irreversible mixing of air masses in the lowermost stratosphere. However, further research should address the seasonal and geographical variability of small–scale, GW–induced shear over the mid-latitude region.

The similarities and differences we find here are certainly model, resolution and parameterization dependent. While ICON demonstrates skill in reproducing GW flux patterns comparable to those in IFS, questions remain as to whether resolved GW amplitudes in the extratropics are fully converged across resolutions, and how parameterized sources interact with the resolved spectrum. To a certain extent, this is supported by the fact that high-resolution simulations have not yet converged when it comes to GWs in the extratropics (Kruse et al., 2022; Polichtchouk et al., 2023; Gupta et al., 2024).

Our results suggest a multiscale cascade in which orographically generated inertia–gravity waves enhance shear, trigger small-scale instabilities, and promote turbulence, thereby enabling vertical energy and momentum transfer. GW-induced shear

emerges as a key driver of UTLS transport, mixing, and CAT occurrence. This warrants further investigation of its regional prevalence and implications for the redistribution of H_2O and O_3 and associated radiative forcing (e.g., Riese et al., 2012), as well as aviation forecasting (e.g., Kim and Chun, 2011; Sharman and Pearson, 2017). Overall, GW-related processes are a key mechanism for interpreting CAT in the extratropical UTLS.

Data availability. The WISE flight data is available on the HALO-DB. The data used for this paper is available on Zenodo (Umbarkar, 2025) (last access: 08 September 2025). ERA5 model level data was retrieved from the MARS archive. The data is also publicly available from Copernicus Climate Change Service (C3S) Climate Data Store using the CDS API. The dataset used is: "ERA5: Fifth generation of ECMWF atmospheric reanalyses of the global climate" https://doi.org/10.24381/cds.143582cf (last access: 08 September 2025). IFS forecast data was retrieved from the MARS archive. The ICON source code is distributed under an institutional license issued by the German Weather Service (DWD). The ICON model output used in this study is available upon reasonable request .

Appendix A: Supporting figures to selected methodology, synoptic situation and hodograph analysis

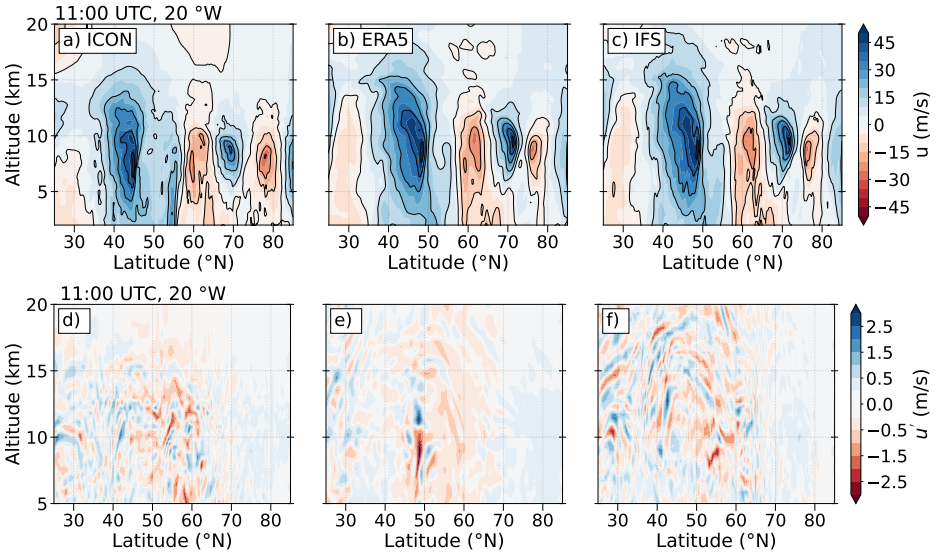


Figure A1. Vertical cross section of zonal wind u (upper panel) and retrieved u perturbations (lower panel) on 23 September 2017 11:00 UTC at 20°W for (a, d) ICON, (b, e) ERA5, and (c, f) IFS.

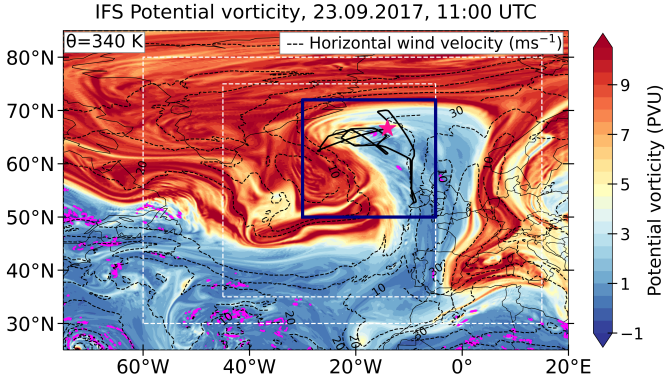


Figure A2. IFS potential vorticity distribution (in PVU) at the 340 K isentropic surface on 23.09.2017 at 11:00 UTC. The dashed lines show the horizontal wind (in m s^{-1}) on 340 K. The thick black line shows the flight path of RF05 and the star marks the aircraft position at 11:00 UTC. Magenta color shows the negative PV values.

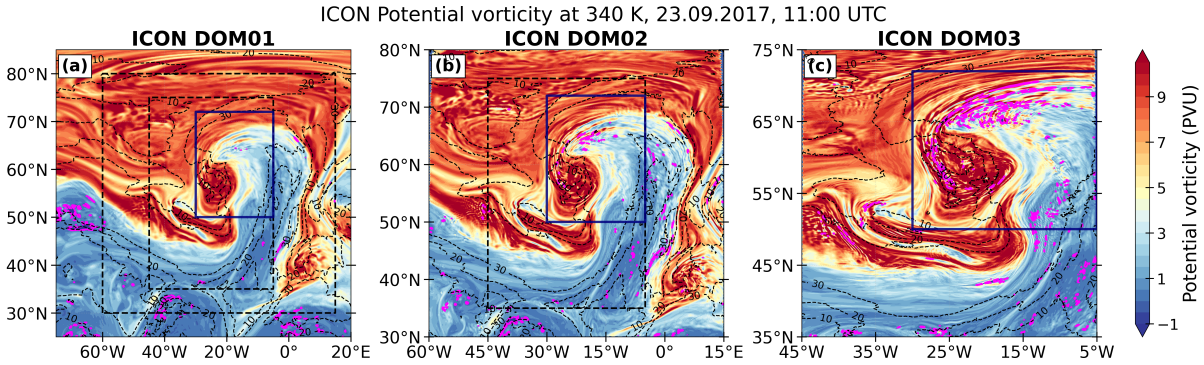


Figure A3. Potential vorticity distribution (in PVU) at the 340 K isentropic surface on 23.09.2017 at 11:00 UTC for three ICON domains: (a) ICON 13 km (b) ICON 6.5 km and (c) ICON 3.3 km. The dashed lines show the horizontal wind (in m s^{-1}) on 340 K. Magenta color shows the negative PV values, while blue box represent analysis domain selected for this study.

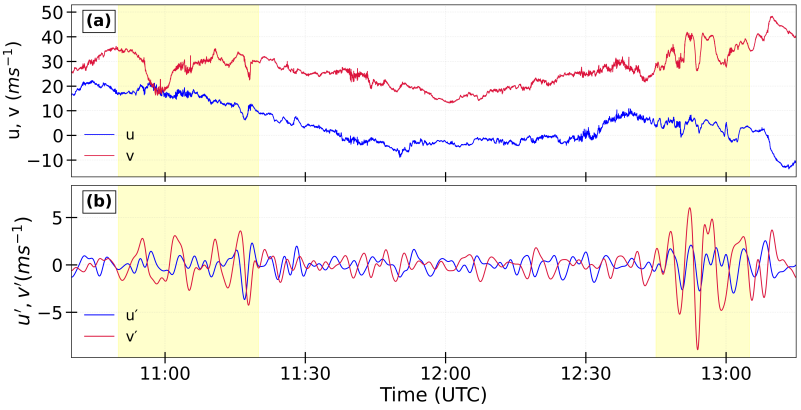


Figure A4. Time series of (a) zonal (u, ms^{-1}; blue) and meridional (v, ms^{-1}; red) wind component from HALO for WISE RF05, the shaded yellow regions same as Fig. 3, whereas panel (b) shows perturbation of u and v obtained from Butterworth filter.

Appendix B: Supporting information to the GW and shear analysis

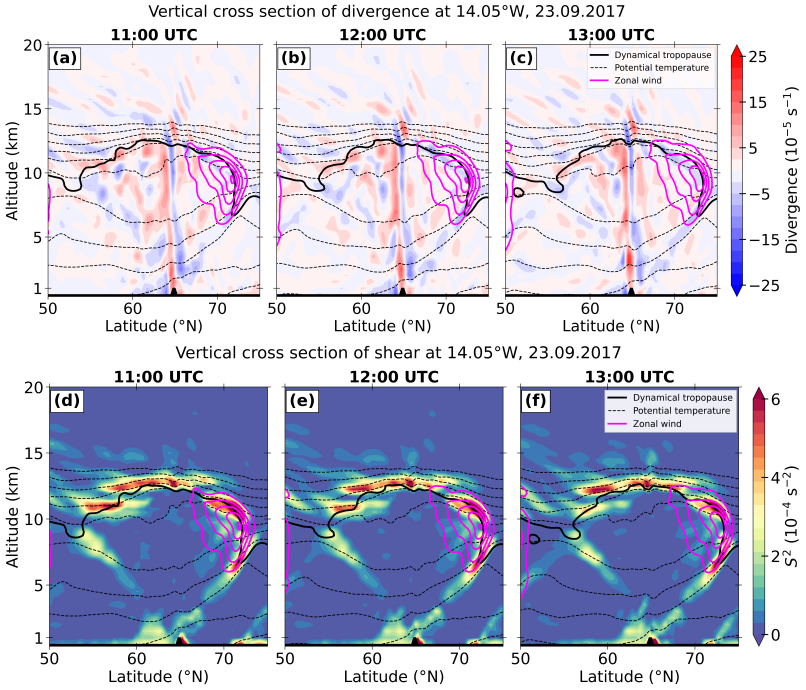


Figure B1. Vertical cross sections of divergence (a-c) and vertical shear (d-f) at longitude 14.05° W for ERA5 data at 11:00 UTC,12:00 UTC and 13:00 UTC. The solid black line represent the 3.5 PVU as a dynamical tropopause whereas dashed lines in lower panel represent the potential temperature starting from 280 K (bottom) to 380 K (top) with 10 K increments.

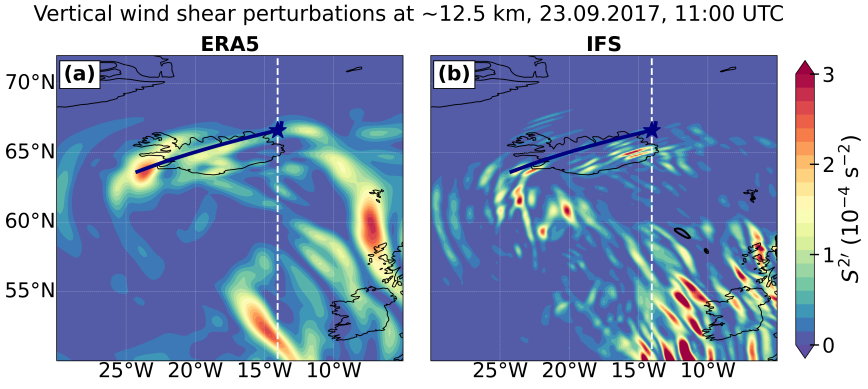


Figure B2. Distribution of vertical wind shear perturbations $S^{2'}$ at 12.5 km altitude for (a) ERA5 and (b) IFS.

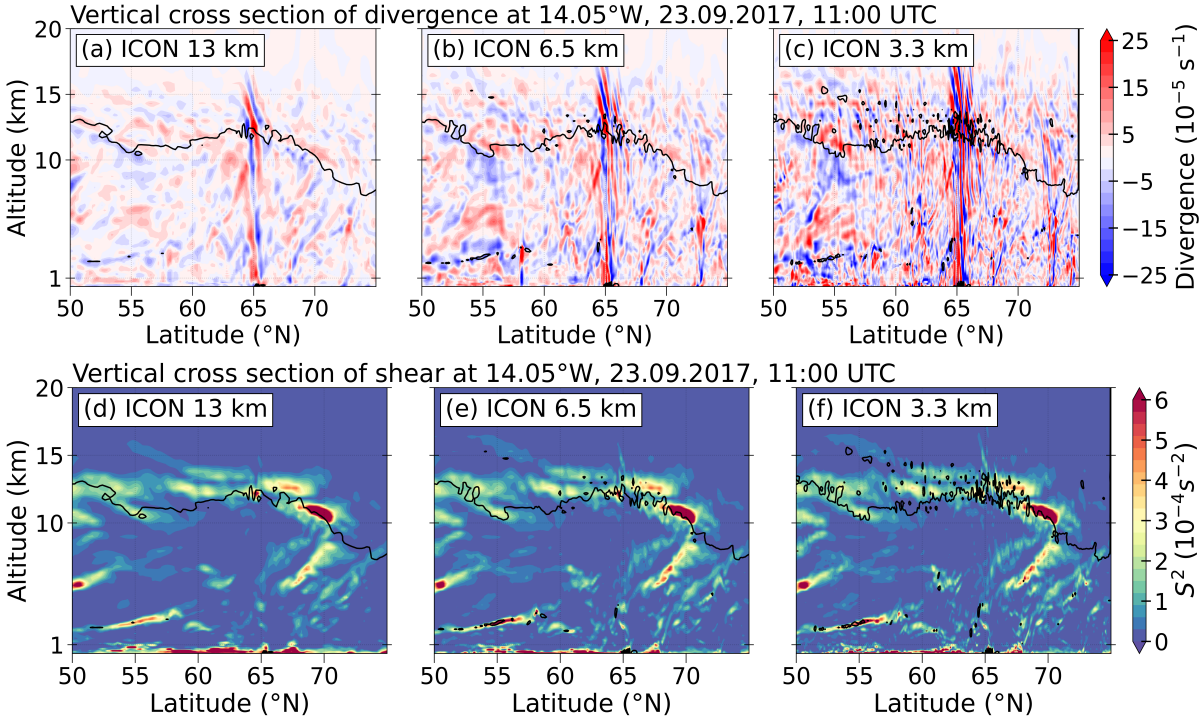


Figure B3. Vertical cross sections of divergence (a-c) and vertical shear (d-f) at longitude 14.05° W for three ICON domains. The solid black line represent the 3.5 PVU as a dynamical tropopause.

Appendix C: Supporting information to the CAT analysis

We use all data points in the LMS i.e., between 3.5 PVU and 380 K, to derive PDF distribution of the small–scale TI1 and TI2 indices. We then calculate the 95th percentile values of these distributions, which are used as threshold values. The resulting TI1 threshold values for ERA5, IFS and ICON are $1.4 \times 10^{-7} s^{-1}$, $2.1 \times 10^{-7} s^{-1}$ and $1.5 \times 10^{-7} s^{-1}$ respectively. There are only minor difference in the threshold observed across the datasets. Given the range of values in PDFs and the differences in the underlying data, the gained thresholds differ only slightly across the datasets, with some differing up to a factor of two. Furthermore, the more GW related index TI2, gained from the inclusion of convergent flow, applies the same threshold criterion as TI1, where the resulting thresholds are $1.5 \times 10^{-7} s^{-1}$, $2.45 \times 10^{-7} s^{-1}$, and $1.5 \times 10^{-7} s^{-1}$ for ERA5, IFS and ICON, respectively. We categorize the CAT levels based on the thresholds: light to moderate from respective 95th percentile threshold, moderate ($7.5 \times 10^{-7} s^{-1}$ to $12 \times 10^{-7} s^{-1}$), and moderate-or-greater ($>12 \times 10^{-7} s^{-1}$), consistent with previous studies (e.g., Ellrod and Knapp, 1992; Thompson and Schultz, 2021).

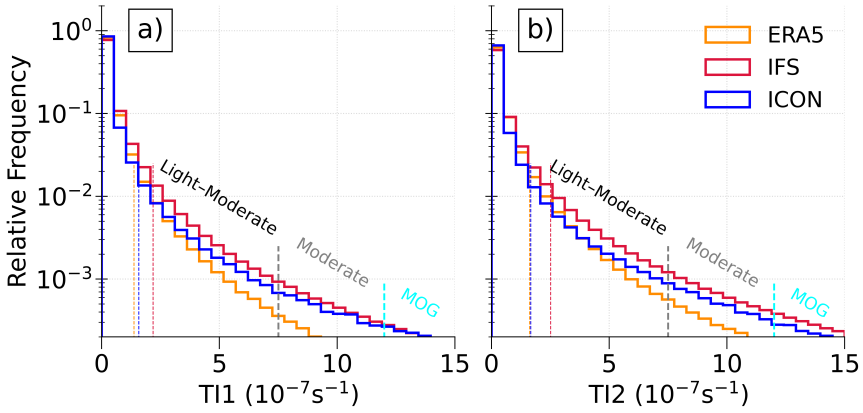


Figure C1. Relative occurrence frequency distribution of (a) TI1 and (b) TI2 for ERA5, IFS and ICON in the LMS domain. Corresponding to histogram, colored dashed lines indicate threshold retrieved as the 95th percentile over the LMS domain that is considered as threshold for light moderate category. Grey and aqua lines represent the threshold for moderate ($7.5\text{-}12 \times 10^{-7} s^{-1}$) and moderate to greater (moderate to greater; $> 12 \times 10^{-7} s^{-1}$) intensity clear air turbulence, respectively.

ICON sensitivity: CAT threshold selection

The relative occurrence frequency distribution of TI1 and TI2 for three ICON nested domains in the LMS is shown in Fig. 17. The threshold criterion is based on 95th percentile for each case in the LMS and is same as in ERA5. Based on this, the resulting TI1 threshold values for simulations with $\Delta x \approx 13$ km, $\Delta x \approx 6.5$ km, and $\Delta x \approx 3.3$ km are $1.5 \times 10^{-7}\,\mathrm{s}^{-1}$, $3.21 \times 10^{-7}\,\mathrm{s}^{-1}$, and $4.03 \times 10^{-7}\,\mathrm{s}^{-1}$, respectively; and for TI2, the resultant threshold values are $1.72 \times 10^{-7}\,\mathrm{s}^{-1}$, $3.75 \times 10^{-7}\,\mathrm{s}^{-1}$, and $4.31 \times 10^{-7}\,\mathrm{s}^{-1}$, respectively. For the comparison across experiments and following the previous studies (e.g., Thompson and Schultz, 2021), the threshold values are kept common for moderate ($7.5\text{–}12 \times 10^{-7}\,\mathrm{s}^{-1}$) and moderate to greater ($>12 \times 10^{-7}\,\mathrm{s}^{-1}$) categories.

Appendix D: Supporting information to "Turbulence diagnostics in a zonal framework"

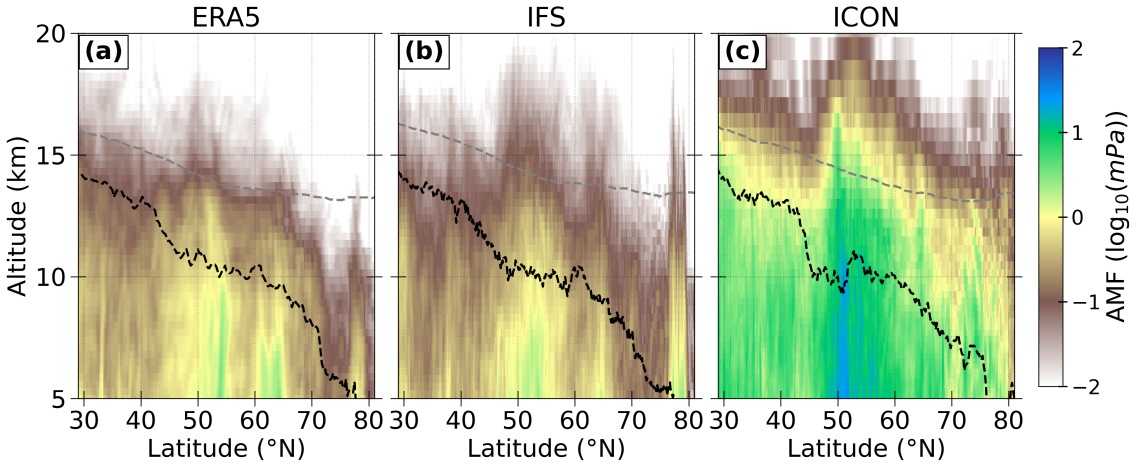


Figure D1. Zonal mean GW absolute momentum flux (AMF, $log_{10}(mPa)$) for (a) ERA5, (b) IFS and (c) ICON ≈13 km.

Author contributions. MU and DK conceptualized the core research questions and goals. CS and AM set up and conducted the ICON simulations. TK, HCL, and PH provided the WISE campaign data. MU performed the data analysis, post-processing, and prepared the initial draft of the manuscript. MU and DK jointly revised and edited the manuscript. All authors contributed to and commented on the manuscript.

Competing interests. The authors have no conflict of interest.

Acknowledgements. This work was funded by the Deutsche Forschungsgemeinschaft (DFG, German Research Foundation) – TRR 301 – Project-ID 428312742: “The tropopause region in a changing atmosphere, https://tpchange.de" (last access: 08 September 2025) sub-project B06. WISE campaign was supported by the German Science Foundation (DFG) within the priority program HALO SPP 1294, (KU 3524/1-1, HO 4225/7-1, and HO 4225/8-1). We gratefully acknowledge the computing time provided on the supercomputer MOGON II at Johannes Gutenberg University Mainz (https://hpc.uni-mainz.de) (last access: 08 September 2025). We further thank Ulrich Achatz and Juerg Schmidli from Goethe-Universität Frankfurt for their valuable comments and feedback on this work.

References

Achatz, U., Alexander, M. J., Becker, E., Chun, H. Y., Dörnbrack, A., Holt, L., Plougonven, R., Polichtchouk, I., Sato, K., Sheshadri, A., Stephan, C. C., Van Niekerk, A., and Wright, C. J.: Atmospheric Gravity Waves: Processes and Parameterization, Journal of the Atmospheric Sciences, 81, 237–262, https://doi.org/10.1175/JAS-D-23-0210.1, 2024.

Alexander, M. J. and Grimsdell, A. W.: Seasonal cycle of orographic gravity wave occurrence above small islands in the Southern Hemisphere: Implications for effects on the general circulation, Journal of Geophysical Research: Atmospheres, 118, https://doi.org/10.1002/2013jd020526, 2013.

Alexander, M. J., Geller, M., McLandress, C., Polavarapu, S., Preusse, P., Sassi, F., Sato, K., Eckermann, S., Ern, M., Hertzog, A., Kawatani, Y., Pulido, M., Shaw, T. A., Sigmond, M., Vincent, R., and Watanabe, S.: Recent developments in gravity-wave effects in climatemodels and the global distribution of gravity-wavemomentum flux from observations and models, Quarterly Journal of the Royal Meteorological Society, 136, 1103–1124, https://doi.org/10.1002/qj.637, 2010.

Appenzeller, C., Holton, J. R., and Rosenlof, K. H.: Seasonal variation of mass transport across the tropopause, Journal of Geophysical Research: Atmospheres, 101, 15 071–15 078, https://doi.org/10.1029/96jd00821, 1996.

Berthet, G., Esler, J. G., and Haynes, P. H.: A Lagrangian perspective of the tropopause and the ventilation of the lowermost stratosphere, Journal of Geophysical Research: Atmospheres, 112, https://doi.org/10.1029/2006jd008295, 2007.

Birner, T.: Fine-scale structure of the extratropical tropopause region, Journal of Geophysical Research Atmospheres, 111, 1–14, https://doi.org/10.1029/2005JD006301, 2006.

Birner, T., Dörnbrack, A., and Schumann, U.: How sharp is the tropopause at midlatitudes?, Geophysical Research Letters, 29, 1–4, https://doi.org/10.1029/2002GL015142, 2002.

Butterworth, S.: On the theory of filter amplifiers, Experimental wireless and the wireless engineer, 7, 536–541, 1930.

Chau, C. H., Hoor, P., and Tost, H.: Simulated mixing in the UTLS by small-scale turbulence using multi-scale chemistry-climate model MECO(n), Atmospheric Chemistry and Physics, 25, 13 123–13 140, https://doi.org/10.5194/acp-25-13123-2025, 2025.

Chau, C. H., Hoor, P., Kaiser, K., and Tost, H.: Parametrizing the mixing by clear air turbulence in the chemistry climate model EMAC and its respective radiative impact, Atmospheric Chemistry and Physics, 26, 3637–3652, https://doi.org/10.5194/acp-26-3637-2026, 2026.

Dörnbrack, A.: Transient Tropopause Waves, Journal of the Atmospheric Sciences, 81, 1647–1668, https://doi.org/10.1175/jas-d-24-0037.1, 2024.

Dörnbrack, A., Bechtold, P., and Schumann, U.: High-Resolution Aircraft Observations of Turbulence and Waves in the Free Atmosphere and Comparison With Global Model Predictions, Journal of Geophysical Research: Atmospheres, 127, https://doi.org/10.1029/2022jd036654, 2022.

Dörnbrack, A., Lachnitt, H., Hoor, P., and Imazio, P. R.: Multiscale Dynamical Processes Shaping a Mixing Line, Journal of Geophysical Research: Atmospheres, 130, https://doi.org/10.1029/2025jd043527, 2025.

Durran, D. R.: Pseudomomentum Diagnostics for Two-Dimensional Stratified Compressible Flow, Journal of Atmospheric Sciences, 52, 3997 – 4009, https://doi.org/10.1175/1520-0469(1995)052<3997:PDFTDS>2.0.CO;2, 1995.

Ellrod, G. P. and Knapp, D. I.: An Objective Clear-Air Turbulence Forecasting Technique: Verification and Operational Use, Weather and Forecasting, 7, 150–165, https://doi.org/10.1175/1520-0434(1992)007<0150:aocatf>2.0.co;2, 1992.

Fritts, D. C. and Alexander, M. J.: Gravity wave dynamics and effects in the middle atmosphere, Reviews of Geophysics, 41, 1–64, https://doi.org/10.1029/2001RG000106, 2003.

Geller, M. A., Alexander, M. J., Love, P. T., Bacmeister, J., Ern, M., Hertzog, A., Manzini, E., Preusse, P., Sato, K., Scaife, A. A., and Zhou, T.: A Comparison between Gravity Wave Momentum Fluxes in Observations and Climate Models, Journal of Climate, 26, 6383–6405, https://doi.org/10.1175/jcli-d-12-00545.1, 2013.

Gomes, M. B., Shapiro, A., Parsons, D. B., and Gebauer, J. G.: Using a Numerical Model to Evaluate a Proposed Mechanism for Nocturnal Low-Level Jets and Ascent over a Warm Tongue, Monthly Weather Review, 153, 1265–1281, https://doi.org/10.1175/mwr-d-24-0111.1, 2025.

Guest, F. M., Reeder, M. J., Marks, C. J., and Karoly, D. J.: Inertia–Gravity Waves Observed in the Lower Stratosphere over Macquarie Island, Journal of the Atmospheric Sciences, 57, 737–752, https://doi.org/10.1175/1520-0469(2000)057<0737:igwoit>2.0.co;2, 2000.

Gultepe, I., Sharman, R., Williams, P. D., Zhou, B., Ellrod, G., Minnis, P., Trier, S., Griffin, S., Yum, S. S., Gharabaghi, B., Feltz, W., Temimi, M., Pu, Z., Storer, L. N., Kneringer, P., Weston, M. J., Chuang, H.-y., Thobois, L., Dimri, A. P., Dietz, S. J., França, G. B., Almeida, M. V., and Neto, F. L. A.: A Review of High Impact Weather for Aviation Meteorology, Pure and Applied Geophysics, 176, 1869–1921, https://doi.org/10.1007/s00024-019-02168-6, 2019.

Gupta, A., Birner, T., Dörnbrack, A., and Polichtchouk, I.: Importance of Gravity Wave Forcing for Springtime Southern Polar Vortex Breakdown as Revealed by ERA5, Geophysical Research Letters, 48, https://doi.org/10.1029/2021GL092762, 2021.

Gupta, A., Sheshadri, A., Alexander, M. J., and Birner, T.: Insights on Lateral Gravity Wave Propagation in the Extratropical Stratosphere From 44 Years of ERA5 Data, Geophysical Research Letters, 51, https://doi.org/10.1029/2024gl108541, 2024.

Hegglin, M. I., Boone, C. D., Manney, G. L., and Walker, K. A.: A global view of the extratropical tropopause transition layer from Atmospheric Chemistry Experiment Fourier Transform Spectrometer O3, H2O, and CO, Journal of Geophysical Research Atmospheres, 114, 1–18, https://doi.org/10.1029/2008JD009984, 2009.

Heller, R., Voigt, C., Beaton, S., Dörnbrack, A., Giez, A., Kaufmann, S., Mallaun, C., Schlager, H., Wagner, J., Young, K., and Rapp, M.: Mountain waves modulate the water vapor distribution in the UTLS, Atmospheric Chemistry and Physics, 17, 14 853–14 869, https://doi.org/10.5194/acp-17-14853-2017, 2017.

Hersbach, H., Bell, B., Berrisford, P., Hirahara, S., Horányi, A., Muñoz-Sabater, J., Nicolas, J., Peubey, C., Radu, R., Schepers, D., Simmons, A., Soci, C., Abdalla, S., Abellan, X., Balsamo, G., Bechtold, P., Biavati, G., Bidlot, J., Bonavita, M., De Chiara, G., Dahlgren, P., Dee, D., Diamantakis, M., Dragani, R., Flemming, J., Forbes, R., Fuentes, M., Geer, A., Haimberger, L., Healy, S., Hogan, R. J., Hólm, E., Janisková, M., Keeley, S., Laloyaux, P., Lopez, P., Lupu, C., Radnoti, G., de Rosnay, P., Rozum, I., Vamborg, F., Villaume, S., and Thépaut, J.: The ERA5 global reanalysis, Quarterly Journal of the Royal Meteorological Society, 146, 1999–2049, https://doi.org/10.1002/qj.3803, 2020.

Holt, L. A., Alexander, M. J., Coy, L., Liu, C., Molod, A., Putman, W., and Pawson, S.: An evaluation of gravity waves and gravity wave sources in the Southern Hemisphere in a 7 km global climate simulation, Quarterly Journal of the Royal Meteorological Society, 143, 2481–2495, https://doi.org/10.1002/qj.3101, 2017.

Holton, J. R., Haynes, P. H., McIntyre, M. E., Douglass, A. R., Rood, R. B., and Pfister, L.: Stratosphere-troposphere exchange, Reviews of Geophysics, 33, 403–439, https://doi.org/10.1029/95RG02097, 1995.

Hooke, W. H.: Gravity Waves, p. 272–288, American Meteorological Society, ISBN 9781935704201, https://doi.org/10.1007/978-1-935704-20-1_12, 1986.

Hoor, P., Gurk, C., Brunner, D., Hegglin, M. I., Wernli, H., and Fischer, H.: Seasonality and extent of extratropical TST derived from in-situ CO measurements during SPURT, Atmospheric Chemistry and Physics, 4, 1427–1442, https://doi.org/10.5194/acp-4-1427-2004, 2004.

Hoor, P., Wernli, H., Hegglin, M. I., and Bönisch, H.: Transport timescales and tracer properties in the extratropical UTLS, Atmospheric Chemistry and Physics, 10, 7929–7944, https://doi.org/10.5194/acp-10-7929-2010, 2010.

Jaeger, E. B. and Sprenger, M.: A Northern Hemispheric climatology of indices for clear air turbulence in the tropopause region derived from ERA40 reanalysis data, Journal of Geophysical Research Atmospheres, 112, 1–13, https://doi.org/10.1029/2006JD008189, 2007.

Jewtoukoff, V., Hertzog, A., Plougonven, R., Cámara, A. d. l., and Lott, F.: Comparison of Gravity Waves in the Southern Hemisphere Derived from Balloon Observations and the ECMWF Analyses, Journal of the Atmospheric Sciences, 72, 3449–3468, https://doi.org/10.1175/jas-d-14-0324.1, 2015.

Jovanovic, G.: Gravity waves as a mechanism of troposphere–stratosphere–mesosphere coupling during sudden stratospheric warming, Atmospheric Chemistry and Physics, 25, 2979–2988, https://doi.org/10.5194/acp-25-2979-2025, 2025.

Kaluza, T., Kunkel, D., and Hoor, P.: Composite analysis of the tropopause inversion layer in extratropical baroclinic waves, Atmospheric Chemistry and Physics, 19, 6621–6636, https://doi.org/10.5194/acp-19-6621-2019, 2019.

Kaluza, T., Kunkel, D., and Hoor, P.: On the occurrence of strong vertical wind shear in the tropopause region: a 10-year ERA5 northern hemispheric study, Weather and Climate Dynamics, 2, 631–651, https://doi.org/10.5194/wcd-2-631-2021, 2021.

Kaluza, T., Kunkel, D., and Hoor, P.: Analysis of Turbulence Reports and ERA5 Turbulence Diagnostics in a Tropopause-Based Vertical Framework, Geophysical Research Letters, 49, https://doi.org/10.1029/2022gl100036, 2022.

Kim, J.-H. and Chun, H.-Y.: Statistics and Possible Sources of Aviation Turbulence over South Korea, Journal of Applied Meteorology and Climatology, 50, 311–324, https://doi.org/10.1175/2010jamc2492.1, 2011.

Kim, J.-H., Sharman, R., Strahan, M., Scheck, J. W., Bartholomew, C., Cheung, J. C. H., Buchanan, P., and Gait, N.: Improvements in Nonconvective Aviation Turbulence Prediction for the World Area Forecast System, Bulletin of the American Meteorological Society, 99, 2295–2311, https://doi.org/10.1175/bams-d-17-0117.1, 2018.

Kim, Y., Eckermann, S. D., and Chun, H.: An overview of the past, present and future of gravity-wave drag parametrization for numerical climate and weather prediction models, Atmosphere-Ocean, 41, 65–98, https://doi.org/10.3137/ao.410105, 2003.

Knox, J. A.: Possible Mechanisms of Clear-Air Turbulence in Strongly Anticyclonic Flows, Monthly Weather Review, 125, 1251–1259, https://doi.org/10.1175/1520-0493(1997)125<1251:pmocat>2.0.co;2, 1997.

Koch, S. E., Jamison, B. D., Lu, C., Smith, T. L., Tollerud, E. I., Girz, C., Wang, N., Lane, T. P., Shapiro, M. A., Parrish, D. D., and Cooper, O. R.: Turbulence and Gravity Waves within an Upper-Level Front, Journal of the Atmospheric Sciences, 62, 3885–3908, https://doi.org/10.1175/jas3574.1, 2005.

Krautstrunk, M. and Giez, A.: The Transition From FALCON to HALO Era Airborne Atmospheric Research, p. 609–624, Springer Berlin Heidelberg, ISBN 9783642301834, https://doi.org/10.1007/978-3-642-30183-4_37, 2012.

Kruse, C. G. and Smith, R. B.: Gravity Wave Diagnostics and Characteristics in Mesoscale Fields, Journal of the Atmospheric Sciences, 72, 4372–4392, https://doi.org/10.1175/jas-d-15-0079.1, 2015.

Kruse, C. G., Alexander, M. J., Hoffmann, L., van Niekerk, A., Polichtchouk, I., Bacmeister, J. T., Holt, L., Plougonven, R., Šácha, P., Wright, C., Sato, K., Shibuya, R., Gisinger, S., Ern, M., Meyer, C. I., and Stein, O.: Observed and Modeled Mountain Waves from the Surface to the Mesosphere near the Drake Passage, Journal of the Atmospheric Sciences, 79, 909–932, https://doi.org/10.1175/jas-d-21-0252.1, 2022.

Kunkel, D., Hoor, P., and Wirth, V.: Can inertia-gravity waves persistently alter the tropopause inversion layer?, Geophysical Research Letters, 41, 7822–7829, https://doi.org/10.1002/2014GL061970, 2014.

Kunkel, D., Hoor, P., and Wirth, V.: The tropopause inversion layer in baroclinic life-cycle experiments: The role of diabatic processes, Atmospheric Chemistry and Physics, 16, 541–560, https://doi.org/10.5194/acp-16-541-2016, 2016.

Kunkel, D., Hoor, P., Kaluza, T., Ungermann, J., Kluschat, B., Giez, A., Lachnitt, H. C., Kaufmann, M., and Riese, M.: Evidence of small-scale quasi-isentropic mixing in ridges of extratropical baroclinic waves, Atmospheric Chemistry and Physics, 19, 12 607–12 630, https://doi.org/10.5194/acp-19-12607-2019, 2019.

Lachnitt, H. C.: Consistent meteorological (ERA5) and chemical (CLaMS) information across airborne measurements over the globe between 1997 and 2023, Zenodo [data set], https://doi.org/10.5281/ZENODO.15076520, (last access: 08 September 2025), 2025.

Lachnitt, H. C., Hoor, P., Kunkel, D., Bramberger, M., Dörnbrack, A., Müller, S., Reutter, P., Giez, A., Kaluza, T., and Rapp, M.: Gravity-wave-induced cross-isentropic mixing: A DEEPWAVE case study, Atmospheric Chemistry and Physics, 23, 355–373, https://doi.org/10.5194/acp-23-355-2023, 2023.

Lane, T. P. and Sharman, R. D.: Gravity wave breaking, secondary wave generation, and mixing above deep convection in a three-dimensional cloud model, Geophysical Research Letters, 33, https://doi.org/10.1029/2006gl027988, 2006.

Lane, T. P., Reeder, M. J., and Clark, T. L.: Numerical Modeling of Gravity Wave Generation by Deep Tropical Convection, Journal of the Atmospheric Sciences, 58, 1249–1274, https://doi.org/10.1175/1520-0469(2001)058<1249:nmogwg>2.0.co;2, 2001.

Lane, T. P., Doyle, J. D., Plougonven, R., Shapiro, M. A., and Sharman, R. D.: Observations and Numerical Simulations of Inertia–Gravity Waves and Shearing Instabilities in the Vicinity of a Jet Stream, Journal of the Atmospheric Sciences, 61, 2692–2706, https://doi.org/10.1175/jas3305.1, 2004.

Lee, D.-B., Chun, H.-Y., and Kim, J.-H.: Evaluation of Multimodel-Based Ensemble Forecasts for Clear-Air Turbulence, Weather and Forecasting, 35, 507–521, https://doi.org/10.1175/waf-d-19-0155.1, 2019.

Lee, J. H., Kim, J., Sharman, R. D., Kim, J., and Son, S.: Climatology of Clear-Air Turbulence in Upper Troposphere and Lower Stratosphere in the Northern Hemisphere Using ERA5 Reanalysis Data, Journal of Geophysical Research: Atmospheres, 128, https://doi.org/10.1029/2022jd037679, 2022.

Lehmann, C. I., Kim, Y.-H., Preusse, P., Chun, H.-Y., Ern, M., and Kim, S.-Y.: Consistency between Fourier transform and small-volume few-wave decomposition for spectral and spatial variability of gravity waves above a typhoon, Atmospheric Measurement Techniques, 5, 1637–1651, https://doi.org/10.5194/amt-5-1637-2012, 2012.

Lott, F. and Miller, M. J.: A new subgrid-scale orographic drag parametrization: Its formulation and testing, Quarterly Journal of the Royal Meteorological Society, 123, 101–127, https://doi.org/10.1002/qj.49712353704, 1997.

Müller, S., Hoor, P., Berkes, F., Bozem, H., Klingebiel, M., Reutter, P., Smit, H. G. J., Wendisch, M., Spichtinger, P., and Borrmann, S.: In situ detection of stratosphere-troposphere exchange of cirrus particles in the midlatitudes, Geophysical Research Letters, 42, 949–955, https://doi.org/10.1002/2014gl062556, 2015.

Olsen, M. A., Douglass, A. R., and Kaplan, T. B.: Variability of extratropical ozone stratosphere–troposphere exchange using microwave limb sounder observations, Journal of Geophysical Research: Atmospheres, 118, 1090–1099, https://doi.org/10.1029/2012jd018465, 2013.

Orr, A., Bechtold, P., Scinocca, J., Ern, M., and Janiskova, M.: Improved middle atmosphere climate and forecasts in the ECMWF model through a non-orographic gravity wave drag parametrization, ECMWF, https://doi.org/10.21957/DM64CMPJ, 2010.

O'sullivan, D. and Dunkerton, T. J.: Generation of Inertia–Gravity Waves in a Simulated Life Cycle of Baroclinic Instability, Journal of Atmospheric Sciences, 52, 3695 – 3716, https://doi.org/10.1175/1520-0469(1995)052<3695:GOIWIA>2.0.CO;2, 1995.

Pan, L. L., Randel, W. J., Gary, B. L., Mahoney, M. J., and Hintsa, E. J.: Definitions and sharpness of the extratropical tropopause: A trace gas perspective, Journal of Geophysical Research: Atmospheres, 109, https://doi.org/10.1029/2004jd004982, 2004.

Pan, L. L., Konopka, P., and Browell, E. V.: Observations and model simulations of mixing near the extratropical tropopause, Journal of Geophysical Research Atmospheres, 111, 1–15, https://doi.org/10.1029/2005JD006480, 2006.

Plougonven, R. and Snyder, C.: Gravity waves excited by jets: Propagation versus generation, Geophysical Research Letters, 32, https://doi.org/10.1029/2005gl023730, 2005.

Plougonven, R. and Zhang, F.: Internal gravity waves from atmospheric jets and fronts, Reviews of Geophysics, 52, 33–76, https://doi.org/10.1002/2012rg000419, 2014.

Plougonven, R., Teitelbaum, H., and Zeitlin, V.: Inertia gravity wave generation by the tropospheric midlatitude jet as given by the Fronts and Atlantic Storm-Track Experiment radio soundings, Journal of Geophysical Research: Atmospheres, 108, https://doi.org/10.1029/2003jd003535, 2003.

Plougonven, R., Hertzog, A., and Teitelbaum, H.: Observations and simulations of a large-amplitude mountain wave breaking over the Antarctic Peninsula, Journal of Geophysical Research Atmospheres, 113, 1–17, https://doi.org/10.1029/2007JD009739, 2008.

Plougonven, R., Hertzog, A., and Alexander, M. J.: Case studies of nonorographic gravity waves over the Southern Ocean emphasize the role of moisture, Journal of Geophysical Research: Atmospheres, 120, 1278–1299, https://doi.org/10.1002/2014jd022332, 2015.

Plougonven, R., Jewtoukoff, V., Cámara, A. d. l., Lott, F., and Hertzog, A.: On the Relation between Gravity Waves and Wind Speed in the Lower Stratosphere over the Southern Ocean, Journal of the Atmospheric Sciences, 74, 1075–1093, https://doi.org/10.1175/jas-d-16-0096.1, 2017.

Polichtchouk, I., van Niekerk, A., and Wedi, N.: Resolved Gravity Waves in the Extratropical Stratosphere: Effect of Horizontal Resolution Increase from O(10) to O(1) km, Journal of the Atmospheric Sciences, 80, 473–486, https://doi.org/10.1175/jas-d-22-0138.1, 2023.

Rapp, M., Kaifler, B., Dörnbrack, A., Gisinger, S., Mixa, T., Reichert, R., Kaifler, N., Knobloch, S., Eckert, R., Wildmann, N., Giez, A., Krasauskas, L., Preusse, P., Geldenhuys, M., Riese, M., Woiwode, W., Friedl-Vallon, F., Sinnhuber, B.-M., Torre, A. d. l., Alexander, P., Hormaechea, J. L., Janches, D., Garhammer, M., Chau, J. L., Conte, J. F., Hoor, P., and Engel, A.: SOUTHTRAC-GW: An Airborne Field Campaign to Explore Gravity Wave Dynamics at the World's Strongest Hotspot, Bulletin of the American Meteorological Society, 102, E871–E893, https://doi.org/10.1175/bams-d-20-0034.1, 2021.

Raschendorfer, M.: The new turbulence parameterization of LM, COSMO Newsletter No. 1, pp. 89–97, 2001.

Riese, M., Ploeger, F., Rap, A., Vogel, B., Konopka, P., Dameris, M., and Forster, P.: Impact of uncertainties in atmospheric mixing on simulated UTLS composition and related radiative effects, Journal of Geophysical Research: Atmospheres, 117, https://doi.org/10.1029/2012jd017751, 2012.

Schwenk, C. and Miltenberger, A.: The role of ascent timescales for warm conveyor belt (WCB) moisture transport into the upper troposphere and lower stratosphere (UTLS), Atmospheric Chemistry and Physics, 24, 14 073–14 099, https://doi.org/10.5194/acp-24-14073-2024, 2024.

Schwenk, C. and Miltenberger, A.: The role of ascent timescales for warm conveyor belt (WCB) moisture transport into the upper troposphere and lower stratosphere (UTLS), Zenodo [data set], https://doi.org/10.5281/ZENODO.14924689, (last access: 08 September 2025), 2025.

Seifert, A.: On the parameterization of evaporation of raindrops as simulated by a one-dimensional rainshaft model, Journal of the Atmospheric Sciences, 65, 3608–3619, https://doi.org/10.1175/2008JAS2586.1, 2008.

Shapiro, M. A.: Further Evidence of the Mesoscale and Turbulent Structure of Upper Level Jet Stream–Frontal Zone Systems, Monthly Weather Review, 106, 1100–1111, https://doi.org/10.1175/1520-0493(1978)106<1100:feotma>2.0.co;2, 1978.

Shapiro, M. A.: Turbulent Mixing within Tropopause Folds as a Mechanism for the Exchange of Chemical Constituents between the Stratosphere and Troposphere, Journal of the Atmospheric Sciences, 37, 994–1004, https://doi.org/10.1175/1520-0469(1980)037<0994:tmwtfa>2.0.co;2, 1980.

Sharman, R., Tebaldi, C., Wiener, G., and Wolff, J.: An Integrated Approach to Mid- and Upper-Level Turbulence Forecasting, Weather and Forecasting, 21, 268–287, https://doi.org/10.1175/waf924.1, 2006.

Sharman, R. D. and Pearson, J. M.: Prediction of Energy Dissipation Rates for Aviation Turbulence. Part I: Forecasting Nonconvective Turbulence, Journal of Applied Meteorology and Climatology, 56, 317–337, https://doi.org/10.1175/jamc-d-16-0205.1, 2017.

Sharman, R. D., Trier, S. B., Lane, T. P., and Doyle, J. D.: Sources and dynamics of turbulence in the upper troposphere and lower stratosphere: A review, Geophysical Research Letters, 39, 1–9, https://doi.org/10.1029/2012GL051996, 2012.

Sharman, R. D., Cornman, L. B., Meymaris, G., Pearson, J., and Farrar, T.: Description and Derived Climatologies of Automated In Situ Eddy-Dissipation-Rate Reports of Atmospheric Turbulence, Journal of Applied Meteorology and Climatology, 53, 1416–1432, https://doi.org/10.1175/jamc-d-13-0329.1, 2014.

Stephan, C. C., Strube, C., Klocke, D., Ern, M., Hoffmann, L., Preusse, P., and Schmidt, H.: Intercomparison of Gravity Waves in Global Convection-Permitting Models, Journal of the Atmospheric Sciences, 76, 2739–2759, https://doi.org/10.1175/jas-d-19-0040.1, 2019a.

Stephan, C. C., Strube, C., Klocke, D., Ern, M., Hoffmann, L., Preusse, P., and Schmidt, H.: Gravity Waves in Global High-Resolution Simulations With Explicit and Parameterized Convection, Journal of Geophysical Research: Atmospheres, 124, 4446–4459, https://doi.org/10.1029/2018jd030073, 2019b.

Strube, C., Ern, M., Preusse, P., and Riese, M.: Removing spurious inertial instability signals from gravity wave temperature perturbations using spectral filtering methods, Atmospheric Measurement Techniques, 13, 4927–4945, https://doi.org/10.5194/amt-13-4927-2020, 2020.

Thompson, C. F. and Schultz, D. M.: The Release of Inertial Instability Near an Idealized Zonal Jet, Geophysical Research Letters, 48, https://doi.org/10.1029/2021gl092649, 2021.

Toghraei, I., Lott, F., Köhler, L., Stephan, C. C., and Alexander, M. J.: Can Parameterizations Reproduce the Gravity Wave Momentum Fluxes and Drag Simulated by a Global High-Resolution Model?, Geophysical Research Letters, 52, https://doi.org/10.1029/2025gl115499, 2025.

Trier, S. B., Sharman, R. D., MuñOz-Esparza, D., and Lane, T. P.: Environment and mechanisms of severe turbulence in a midlatitude cyclone, Journal of the Atmospheric Sciences, 77, 3869–3889, https://doi.org/10.1175/JAS-D-20-0095.1, 2020.

Umbarkar, M.: Data used for paper "Evidence of gravity wave contribution to vertical shear and mixing in the lower stratosphere: a WISE case study", Zenodo [data set], https://doi.org/10.5281/ZENODO.17227439, 2025.

Umbarkar, M. and Kunkel, D.: Contribution of gravity waves to shear in the extratropical lowermost stratosphere: insights from idealized baroclinic life cycle experiments, Atmospheric Chemistry and Physics, 25, 10 159–10 182, https://doi.org/10.5194/acp-25-10159-2025, 2025.

Wang, M. and Fu, Q.: Stratosphere-Troposphere Exchange of Air Masses and Ozone Concentrations Based on Reanalyses and Observations, Journal of Geophysical Research: Atmospheres, 126, https://doi.org/10.1029/2021jd035159, 2021.

Wang, S. and Zhang, F.: Sensitivity of Mesoscale Gravity Waves to the Baroclinicity of Jet-Front Systems, Monthly Weather Review, 135, 670–688, https://doi.org/10.1175/mwr3314.1, 2007.

Wei, J. and Zhang, F.: Mesoscale gravity waves in moist baroclinic jet-front systems, Journal of the Atmospheric Sciences, 71, 929–952, https://doi.org/10.1175/JAS-D-13-0171.1, 2014.

Wei, J., Zhang, F., and Richter, J. H.: An Analysis of Gravity Wave Spectral Characteristics in Moist Baroclinic Jet–Front Systems, Journal of the Atmospheric Sciences, 73, 3133–3155, https://doi.org/10.1175/jas-d-15-0316.1, 2016.

Wei, J., Zhang, F., Richter, J. H., Alexander, M. J., and Sun, Y. Q.: Global Distributions of Tropospheric and Stratospheric Gravity Wave Momentum Fluxes Resolved by the 9-km ECMWF Experiments, Journal of the Atmospheric Sciences, 79, 2621–2644, https://doi.org/10.1175/jas-d-21-0173.1, 2022.

Weyland, F., Hoor, P., Kunkel, D., Birner, T., Plöger, F., and Turhal, K.: Long-term changes in the thermodynamic structure of the lowermost stratosphere inferred from reanalysis data, Atmospheric Chemistry and Physics, 25, 1227–1252, https://doi.org/10.5194/acp-25-1227-2025, 2025.

Whiteway, J. A., Pavelin, E. G., Busen, R., Hacker, J., and Vosper, S.: Airborne measurements of gravity wave breaking at the tropopause, Geophysical Research Letters, 30, 2–6, https://doi.org/10.1029/2003GL018207, 2003.

Whiteway, J. A., Klaassen, G. P., Bradshaw, N. G., and Hacker, J.: Transition to turbulence in shear above the tropopause, Geophysical Research Letters, 31, 2–5, https://doi.org/10.1029/2003GL018509, 2004.

Yoshida, L., Tomikawa, Y., Ejiri, M. K., Tsutsumi, M., Kohma, M., and Sato, K.: Large-Amplitude Inertia Gravity Waves Over Syowa Station: Comparison of PANSY Radar and ERA5 Reanalysis Data, Journal of Geophysical Research: Atmospheres, 129, https://doi.org/10.1029/2023jd040490, 2024.

Zängl, G., Reinert, D., Rípodas, P., and Baldauf, M.: The <scp>ICON</scp> (ICOsahedral Non-hydrostatic) modelling framework of <scp>DWD</scp> and <scp>MPI-M</scp>: Description of the non-hydrostatic dynamical core, Quarterly Journal of the Royal Meteorological Society, 141, 563–579, https://doi.org/10.1002/qj.2378, 2014.

Zhang, F., Davis, C. A., Kaplan, M. L., and Koch, S. E.: Wavelet analysis and the governing dynamics of a large-amplitude mesoscale gravity-wave event along the East Coast of the United States, Quarterly Journal of the Royal Meteorological Society, 127, 2209–2245, https://doi.org/10.1002/qj.49712757702, 2001.

Zhang, F., Wei, J., Zhang, M., Bowman, K. P., Pan, L. L., Atlas, E., and Wofsy, S. C.: Aircraft measurements of gravity waves in the upper troposphere and lower stratosphere during the START08 field experiment, Atmospheric Chemistry and Physics, 15, 7667–7684, https://doi.org/10.5194/acp-15-7667-2015, 2015a.

Zhang, W., Peng, J., Zhang, W., Wang, S., Li, Z., and Hanyan, W.: Sensitivity of Gravity Wave Momentum Flux Estimates on Separation Methods, Monthly Weather Review, 153, 1721–1742, https://doi.org/10.1175/mwr-d-24-0272.1, 2025.

Zhang, Y., Zhang, S., Huang, C., Huang, K., Gong, Y., and Gan, Q.: The interaction between the tropopause inversion layer and the inertial gravity wave activities revealed by radiosonde observations at a midlatitude station, Journal of Geophysical Research: Atmospheres, 120, 8099–8111, https://doi.org/10.1002/2015jd023115, 2015b.

Zhang, Y., Zhang, S., Huang, C., Huang, K., and Gong, Y.: The Tropopause Inversion Layer Interaction With the Inertial Gravity Wave Activities and Its Latitudinal Variability, Journal of Geophysical Research: Atmospheres, 124, 7512–7522, https://doi.org/10.1029/2019JD030309, 2019.

Zülicke, C. and Peters, D.: Simulation of inertia-gravity waves in a poleward-breaking Rossby wave, Journal of the Atmospheric Sciences, 63, 3253–3276, https://doi.org/10.1175/JAS3805.1, 2006.